

# Lawrence Berkeley National Laboratory

## LBL Publications

### Title

Top-casing electric-source method for imaging hydraulically active fracture zones

### Permalink

<https://escholarship.org/uc/item/1fw648qb>

### Authors

Um, Evan Schankee

Kim, Jihoon

Wilt, Michael

et al.

### Publication Date

2018-08-27

### DOI

10.1190/segam2018-2996216.1

Peer reviewed

1 **FINITE ELEMENT ANALYSIS OF TOP-CASING ELECTRIC SOURCE METHOD FOR**  
2 **IMAGING HYDRAULICALLY-ACTIVE FRACTURE ZONES**

3

4

5

6

7

8

9

10 **LIST OF AUTHORS:**

11 Evan Schankee Um, Earth and Environmental Sciences Area, Lawrence Berkeley National Laboratory,  
12 evanum@gmail.com and esum@lbl.gov

13 Jihoon Kim, Harold Vance Department of Petroleum Engineering, Texas A&M University,  
14 jihoon.kim@tamu.edu

15 Michael J. Wilt, Earth and Environmental Sciences Area, Lawrence Berkeley National Laboratory,  
16 mwilt@lbl.gov

17 Michael Commer, Earth and Environmental Sciences Area, Lawrence Berkeley National Laboratory,  
18 mcommer@lbl.gov

19 Seung-Sep Kim, Department of Geology and Earth Environmental Sciences, Chungnam National  
20 University, Daejeon, South Korea, seungsep@cnu.ac.kr

## 1 **ABSTRACT**

2 Imaging hydraulically-active fracture zones (HAFZ) is of paramount importance to subsurface resource  
3 extraction, geological storage and hazardous waste disposal. We present advanced 3D finite-element (FE)  
4 electrical imaging algorithms for HAFZ in the presence of a steel-cased well. The algorithms employ  
5 tetrahedral FE meshes in the simulation domain and coarse rectangular finite-difference (FD) meshes in  
6 the imaging domain. This heterogeneous dual-mesh approach is well suited to modeling multi-scale earth  
7 model due to steel-cased wells. We show that the algorithms accurately and efficiently simulate surface  
8 electric field measurements over a 3D HAFZ at depth when one end point of a surface electric source is  
9 connected to a wellhead. For brevity, this configuration is called the top-casing electric source method.  
10 By replacing a hollow cased well with a solid prism, we improve our computational efficiency without  
11 affecting the solution accuracy. The sensitivity of the top-casing source method to HAFZ highly depends  
12 on the continuity of a steel-cased well, because it makes currents preferentially flow to HAFZ. The  
13 sensitivity also depends on conductivity structures around the well because they control current leaking  
14 from the steel-cased well. We show that the method can image a localized HAFZ and detect changes in its  
15 width and height. The imaging results are improved when a volume of the imaging domain is constrained  
16 from geomechanical perspectives. A primary advantage of the method is the fact that both sources and  
17 receivers are placed on the surface, thus not interrupting well operation.

## 18 **INTRODUCTION**

19 Imaging hydraulically active fracture zones (HAFZ) is an important topic in applied geophysics. For  
20 example, hydraulic fracturing and stimulation have been widely used for enhancing production in oil, gas  
21 and geothermal fields (Zoback 2007; Zoback et. al. 2010). Traditional borehole methods are sensitive to  
22 deep HAFZ, but their sensitivity is often limited to the vicinity of the well. Thus, they cannot tell us about  
23 an overall hydraulically stimulated volume of subsurface. The most often used method for characterizing

1 HAFZ in a reservoir scale would be micro-earthquake (MEQ) methods (Warpinski et al. 2005; Vermilyen  
2 and Zoback, 2011). By analyzing MEQ event locations, we can estimate the stimulation volume.  
3 However, MEQ-based mapping highly depends on initial velocity models, which we do not know well,  
4 leaving uncertainties. More importantly, MEQ event locations do not necessarily correlate with active  
5 fluid pathways and thus, provide only a portion of the answer about estimating overall HAFZ (Hoversten  
6 et al, 2015).

7 It is also important to image deep HAFZ in geological storage sites such as CO<sub>2</sub> sequestration and  
8 hazardous waste disposal sites. During their injection phase, MEQ events are often recorded and can be  
9 utilized for imaging fluid movements and monitoring potential leakage. However, after the injection  
10 phase, the magnitudes of MEQ are often too small to be reliably recorded and interpreted in practice  
11 (Johnston and Shralow, 2011). Active-source seismic methods can also be considered an effective tool  
12 for the monitoring goal. However, their major limitation is long acquisition time and high processing cost.

13 Electrical and electromagnetic (EM) methods are sensitive to pore fluids and thus have the potential to  
14 directly sense a HAFZ, complementing MEQ and active source seismic monitoring. To ensure the  
15 sufficient sensitivity of the methods to deep HAFZ, one can consider injecting highly-conductive saline  
16 fluid or fluid with electromagnetically contrasting tracers (e.g. Moridis and Oldenburg, 2001; Rahmani et  
17 al., 2014; Kim et al., 2014). Such fluid and tracers can raise the magnitude of weak anomalous signals  
18 from HAFZ to a detectable level. It is also proposed to use a steel-cased well as a boosting electric source  
19 that directly charges HAFZ (Schenkel and Morrison, 1994; Marsala et al., 2014; Commer et al., 2015;  
20 Hoversten et al., 2015; Um et al., 2015; Patzer et al., 2017). The sensitivity analysis of the approaches  
21 proposed above has been numerically carried out with simple inflated fracture geometries (Weiss et al.,  
22 2016).

1 In this paper, we numerically evaluate a surface-based electrical method with a steel-cased well for  
2 detecting and imaging HAFZ. In our survey configuration, one end point of a surface electric dipole  
3 source is connected to the top of a steel-cased well to directly charge HAFZ around the well. The other  
4 point of the electric dipole source is grounded sufficiently away from the cased well. The electric fields  
5 are measured on the surface. For simplicity, we call this configuration the top-casing electric source  
6 method. The potential advantage of the method is to characterize HAFZ without requiring well  
7 intervention because both sources and receivers are placed on the surface. This advantage makes the  
8 proposed electrical method fast and economic in hydraulic fracturing operations and safe in hazardous  
9 waste disposal sites.

10 The remainder of this paper is organized as follows. First, we describe a 3D finite-element forward and  
11 inverse modeling algorithm for the electric resistivity method in the presence of a steel-cased well. To  
12 handle the multi-scale DC modeling associated with the presence of the steel-cased well, we introduce a  
13 dual-mesh-based algorithm that utilizes structured finite-difference (FD) imaging meshes and unstructured  
14 finite-element (FE) simulation meshes. The effectiveness of the dual-mesh approach for modeling a steel-  
15 cased well is discussed. Second, we present a simplified version of a steel-cased well model and show its  
16 accuracy and efficiency. Third, using the algorithms, we evaluate the detection sensitivity of the top-  
17 casing electrical source method for several simple 3D HAFZ. Finally, we show the imaging sensitivity of  
18 the method through inversion experiments as the final proof-of-concept analysis step.

## 19 **FORWARD MODELING OF 3D ELECTRICAL RESISTIVITY METHOD**

20 In this paper, we employ a 3D FE electrical resistivity modeling algorithm described in Um et al.  
21 (2010). The governing equation of the electric resistivity method is given as Poisson's equation

$$\nabla \cdot (\sigma(\mathbf{r}) \nabla \phi(\mathbf{r})) = - \nabla \cdot \mathbf{j}_s(\mathbf{r}), \quad (1)$$

22 where  $\phi(\mathbf{r})$  is a potential at position  $\mathbf{r}$ ,  $\sigma(\mathbf{r})$  is electrical conductivity, and  $\mathbf{j}_s$  is an electric source.

1 We discretize the computational domain with tetrahedral meshes. To develop the weak statement,  
 2 equation 1 is multiplied by a weighting function  $\omega(\mathbf{r})$  and is integrated over the volume of a tetrahedral  
 3 element, resulting in

$$\iiint_{V^e} \omega^e(\mathbf{r}) \nabla \cdot (\sigma^e(\mathbf{r}) \nabla \phi^e(\mathbf{r}) + \nabla \cdot \mathbf{j}_s(\mathbf{r})) dv = 0, \quad (2)$$

4 The superscript  $e$  indicates the  $e^{\text{th}}$  tetrahedral element.  $V^e$  is the volume of the  $e^{\text{th}}$  tetrahedral element.

5 The unknown potential at  $\mathbf{r}$  inside the  $e^{\text{th}}$  element is interpolated using the set of four Lagrange

6 polynomials  $n_i^e(\mathbf{r})$  (Jin, 2015)

$$\phi^e(\mathbf{r}) = \sum_{i=1}^4 \phi_i^e n_i^e(\mathbf{r}), \quad (3)$$

7 where  $\phi_i^e$  is the potential at the  $i^{\text{th}}$  node of the  $e^{\text{th}}$  element.

8 We also use the same Lagrange polynomials as the weighting function  $\omega(\mathbf{r})$  in equation 3. Thus,

9 substituting equation 3 into equation 2 and replacing  $\omega(\mathbf{r})$  by  $n_i^e(\mathbf{r})$  result in

$$\mathbf{M}^e \mathbf{u}^e = \mathbf{s}^e \quad (4)$$

10 ,where

$$\mathbf{M}_{ij}^e = \iiint_{V^e} \sigma^e(\mathbf{r}) \left( \frac{\partial n_i^e}{\partial x} \frac{\partial n_j^e}{\partial x} + \frac{\partial n_i^e}{\partial y} \frac{\partial n_j^e}{\partial y} + \frac{\partial n_i^e}{\partial z} \frac{\partial n_j^e}{\partial z} \right) dV, \quad (5)$$

(i,j) element of

$$i \text{ element of } \mathbf{u}^e = [\phi_1^e \quad \phi_2^e \quad \phi_3^e \quad \phi_4^e], \quad (6)$$

$$i \text{ element of } \mathbf{s}^e = \iiint_{V^e} n_i^e(\mathbf{r}) \nabla \cdot \mathbf{j}_s(\mathbf{r}) dv, \quad (7)$$

1 Equation 4 is considered local because it comes from each tetrahedral element. Using the node  
2 connectivity information, local matrix equations from individual elements are assembled into a single  
3 global matrix equation.

4 The resulting system of FE equations is symmetric positive definite. Note that the system matrix is  
5 typically ill-conditioned because the contrast in conductivity across the air-casing interface can be larger  
6 than ten orders of magnitude and also because the discretization of a hollow cased well in a deep earth  
7 model requires mixing millimeter-scale elements with kilometer-scale ones (Um et al., 2015). Our choice  
8 of numerical linear algebra for equation 4 is sparse Cholesky factorization and subsequent backward and  
9 forward substitution (Davis, 2006). After the total potential is determined at each tetrahedral node, the  
10 potential difference at two arbitrary end-points of a finite-long electric dipole receiver is interpolated and  
11 divided by the length of the receiver.

## 12 **INVERSE MODELING ALGORITHM WITH STEEL-CASED WELL**

13 Our inversion implementation described here is based on a general frequency-domain EM inversion  
14 framework. An objective functional is given as

$$\Phi = [\mathbf{D}(\mathbf{d}_{\text{obs}} - \mathbf{d}_{\text{pred}})]^T [\mathbf{D}(\mathbf{d}_{\text{obs}} - \mathbf{d}_{\text{pred}})] + \lambda(\mathbf{W}\boldsymbol{\sigma})^T (\mathbf{W}\boldsymbol{\sigma}), \quad (8)$$

15 where  $\mathbf{D}$  is a data weighting matrix,  $\mathbf{d}_{\text{obs}}$  and  $\mathbf{d}_{\text{pred}}$  are observed and predicted DC data, respectively,  $\mathbf{W}$  is  
16 a regularization matrix defined by FD approximation to Laplacian operator, and  $\boldsymbol{\sigma}$  is a conductivity  
17 model.  $\lambda$  is a regularization parameter.

18 Our inversion algorithm employs a limited-memory Broyden–Fletcher–Goldfarb–Shanno (L-BFGS)  
19 algorithm (Nocedal and Wright, 2006). Inside L-BFGS, a Cholesky factor for equation 4 is re-used to  
20 compute a search direction vector. Accordingly, one inversion iteration requires only one new  
21 factorization if the initial trial step satisfies sufficient decrease of  $\Phi$ . If the trial step fails to sufficiently

1 decrease  $\Phi$ , a line search algorithm performs back-tracking. When multiple sources are used, they share  
2 the factored matrices. To prevent conductivity overshoots in the course of inversion, the conductivity  
3 model is bounded by a logarithmic transformation function (Newman and Alumbaugh, 2000).

4 To accurately and efficiently model a steel-cased well, our inversion scheme includes three  
5 characteristics. First, we use different meshes in the model and simulation domain. Note that dual mesh  
6 approaches have been widely used in EM imaging (Commer and Newman, 2008, Egbert and Kelbert,  
7 2012; Yang et al., 2014; Grayver, 2015; Yang et al., 2016). However, our dual mesh approach is distinct  
8 from others since we use a dual mesh approach with heterogeneous mesh types. Coarse rectangular FD  
9 meshes are used to define the model space (i.e. FD model meshes), whereas fine tetrahedral FE meshes  
10 (i.e. FE simulation meshes) are used to compute forward solutions and subsequent gradient vectors. The  
11 motivation behind the FE-FD dual mesh approach is multifold. First, by using the tetrahedral FE  
12 simulation meshes, the simulation domain is highly refined inside and around wells but remains coarse  
13 elsewhere, leading to efficient forward modeling in the presence of wells (Um et al., 2015). This is a  
14 prime advantage of our FE-FD dual mesh approach over a traditional FD-FD dual mesh approach where  
15 local refinements in simulation meshes extend both horizontally and vertically. Second, it is practical to  
16 use rectangular FD meshes in the model domain. For example, visualization and analysis of tetrahedral  
17 meshes are cumbersome and daunting especially when millimeter scale elements for wells are mixed with  
18 kilometer scale elements for regional geology. Rapid and accurate display of large multi-scale tetrahedral  
19 meshes is currently an active research area in both earth sciences and computer sciences. In contrast, the  
20 use of the structured FD model domain allows us to easily and rapidly visualize and analyze EM imaging  
21 results even in the course of inversion. This is a major practical advantage of our FE-FD dual mesh  
22 approach over single mesh FE inversion approaches and FD-FD approaches.

23 Second, we define two mapping matrices that connect one meshes with the other meshes:  $\mathbf{M}_{\text{FE2FD}}$  and  
24  $\mathbf{M}_{\text{FD2FE}}$  (Um et al., 2017).  $\mathbf{M}_{\text{FD2FE}}$  is  $N_{\text{FE}}$ -by- $N_{\text{FD}}$ , where  $N_{\text{FD}}$  and  $N_{\text{FE}}$  are the number of cells in the FD



1 meshes and the number of tetrahedra in the FE meshes, respectively. Its  $(i,j)$  element is a ratio of an  
2 intersectional volume of the  $i^{\text{th}}$  FE element and the  $j^{\text{th}}$  FD cell to the volume of the  $i^{\text{th}}$  FE element. In  
3 contrast,  $\mathbf{M}_{\text{FE2FD}}$  is a reverse operator of  $\mathbf{M}_{\text{FD2FE}}$ . Its size is  $N_{\text{FD}}$ -by- $N_{\text{FE}}$ . Its  $(i,j)$  element is a ratio of an  
4 intersectional volume of the  $i^{\text{th}}$  FD cell and the  $j^{\text{th}}$  FE element to the volume of the  $i^{\text{th}}$  FD cell. Therefore,  
5  $\mathbf{M}_{\text{FD2FE}}$  and  $\mathbf{M}_{\text{FE2FD}}$  map  $\sigma$  from FD to FE and from FD to FE, respectively, being able to use  
6 heterogeneous mesh types in the model and simulation domain. More details on the two mapping  
7 matrices can be found in Appendix.

8 Third, after L-BFGS computes a search direction vector,  $\mathbf{M}_{\text{FE2FD}}$  maps the vector from FE to FD.  
9 Before it is mapped to FD, its elements that correspond to the steel-cased wells are zeroed. The L-BFGS  
10 line search is performed in the FD model space to find a next conductivity model that decreases  $\Phi$ . When  
11 a candidate FD model with a trial step length is formed,  $\mathbf{M}_{\text{FD2FE}}$  maps the FD model to the FE simulation  
12 meshes. Note that the resulting FE model does not yet include the steel-cased well because the FD model  
13 in the model space does not include it. Therefore, at this point, the conductivity of the steel-cased well is  
14 assigned to the FE elements. Accordingly, the FD model space does not have fine grids for the steel-cased  
15 well but remains coarse, which is important for stable electrical resistivity imaging with a limited number  
16 of electrode receivers. In contrast, the FE modeling uses fine meshes, includes the steel-cased well, and  
17 accurately simulates EM responses to the wells. The implementation steps for our inversion are  
18 summarized below.

19 (1) Choose a starting FD/FE model.

20 (2) If it is a FD model, map it from FD to FE space using  $\mathbf{M}_{\text{FD2FE}}$  and add prescribed cased wells to the  
21 FE model.

22 (3) Perform forward modeling and gradient calculation for the current model in the FE space by solving  
23 equation 4.

- 1 Repeat:
- 2 (4) L-BFGS determines a search direction vector.
- 3 (5) Set elements of the vector that correspond to the cased well to zero.
- 4 (6) Map the vector from FE to FD space using  $\mathbf{M}_{\text{FE2FD}}$ .
- 5 Repeat:
- 6 (7) Create a candidate FD model with a trial step length.
- 7 (8) Map the candidate model from FD to FE using  $\mathbf{M}_{\text{FD2FE}}$  and add the cased well to FE.
- 8 (9) Perform forward modeling and gradient calculation for the candidate model in the FE space.
- 9 (10) If  $\Phi$  does not sufficiently decrease, choose a new trial step length.
- 10 Until  $\Phi$  sufficiently decreases
- 11 Until stop criteria for inversion are met

## 12 **MODELING OF TOP-CASING ELECTRIC SOURCE METHOD**

13 The FE forward modeling algorithm with a direct solver has been proven accurate for computing  
14 electric and EM responses to an earth model that features small-scale geometry and extreme conductivity  
15 contrast of a steel-cased well (Commer et al., 2015; Um et al., 2015). Fine tetrahedral meshes are used to  
16 accurately discretize arbitrarily complex fracture and well geometries and coarse meshes elsewhere.  
17 However, the direct discretization of multiple long (e.g. a few kilometers) hollow cased wells requires a  
18 number of tiny elements (e.g. a few ten million unknowns). Thus, modeling complex well structures with  
19 direct solvers is often prohibitively expensive. In most cases, the direct FE discretization is useful for

1 generating reference responses to a cased well but is not practical enough for inverse modeling where a  
2 number of forward modeling needs to be completed.

3 To practically model a steel-cased well in the 3D Cartesian coordinate system, several approximation  
4 approaches have recently been proposed. For example, a hollow well can be approximated with a prism  
5 (Weiss et al., 2015; Puzyrev et al., 2016). Its conductivity value is determined such that the cross-  
6 sectional conductance of the prism is kept same as the hollow well. The well can also be replaced with a  
7 series of small electric dipoles along the well in the DC and frequency domain (Cuevas, 2014;  
8 Nieuwenhuis et al., 2015). Weiss (2017) introduces a hierarchical electrical conductivity model for  
9 representing complex steel infrastructures and fractures at low computational cost. The accuracy of the  
10 approximation methods depends on various factors including background geology, source types and  
11 frequencies, well completion designs and distribution, distances between wells, sources and receivers and  
12 others. Therefore, one needs to use an approximation method in its scope and compare approximate  
13 solutions with reference solutions.

14 Of the approximation methods above, our choice is to replace a hollow steel-cased well by a prism.  
15 Before we present detection and imaging sensitivity of the top-casing electric source method to HAFZ in  
16 the next sections, we first show its accuracy and effectiveness in the scope of our modeling problem. As  
17 shown in **Figure 1**, the size of a prism is set to the outer diameter of the casing. We use the mesh-  
18 generating software, TetGen (Si, 2015) to generate tetrahedral meshes. **Figure 2** shows that the two  
19 models produce nearly identical responses. The relative differences between the hollow steel-cased well  
20 and the prism rapidly decrease with increasing distance from the wells. This indicates that the detailed  
21 geometry of the well's outer surface becomes less important as a receiver position becomes distant from  
22 the well. After the replacement, the number of elements reduces from 8,421,559 to 745,151 elements,  
23 showing the effective reduction in modeling problem size without affecting the solution accuracy.

1 Equation 4 for the model shown in **Figure 1b** is solved in about 3 minutes using 3.40GHz Intel Skylake  
2 processor, which is fast enough for forward and inverse modeling experiments in the next section.

3 In the next example, we consider a 1km long hollow steel-cased well and its corresponding cylinder and  
4 prisms. For independent verification, we compute surface electric DC responses with a Poisson solver that  
5 is embedded into the 3D FD time-domain modeling algorithm (Commer and Newman, 2004; Commer et  
6 al., 2015). Because FD and FE algorithms are different numerical solution approaches for the same  
7 physics, the agreement between FE and FD solutions will show not only the accuracy of our FE algorithm  
8 but also the validity of the prism approximation.

9 **Figure 3** shows a cross-sectional view of 1) a 1km long hollow steel-cased well, 2) its corresponding  
10 solid cylinder and 3) rectangular prism. One end point of an 870m long electric dipole source is  
11 connected with the surface of the steel-cased well and its alternatives. The background conductivity is set  
12 to 0.0333 S/m. Their surface electric field responses are shown in **Figure 4a**. Their relative differences  
13 with respect to the hollow well model are plotted in **Figure 4b**. For comparison, we also compute the  
14 electric field responses to the rectangular prism model using the FE algorithm described in this  
15 manuscript. The resulting FD and FE solutions agree well with each other. For example, the hollow steel-  
16 cased well and the solid cylinder (both FD models) produce nearly identical responses. When the steel-  
17 cased well is replaced with the rectangular prism, some numerical errors are introduced, but they are  
18 sufficiently small (less than 1.5%). The relative differences between the hollow steel-cased well model  
19 and its FD cylinder and prism models decrease with increasing distance from the well. The FE solution to  
20 the rectangular prism also agrees well with the three FD solutions, showing both the accuracy of the FE  
21 modeling algorithm and the validity of the casing approximation approach in the scope of our modeling  
22 problem.

## 23 **FORWARD SENSITIVITY OF TOP-CASING ELECTRIC SOURCE METHOD TO HAFZ**

1 **Figure 5** shows a top-casing electric source configuration used in this study where one end point of the  
2 electric source is directly connected to the well head and the other end point is grounded sufficiently  
3 distant (2km) from the well head. A 2km long array of  $x$ -oriented electric receivers is placed along the  $+x$   
4 direction at  $y=0\text{m}$  (survey line 1) and a 4km long array of  $y$ -oriented electric receivers along the  $\pm y$   
5 direction at  $x=2\text{km}$  (survey line 2). We consider an L-shaped well for simplicity. The vertical part of the  
6 well is 1.6 km deep and the horizontal part 400 m long. The casing is  $5 \cdot 10^6$  (S/m) conductive and its  
7 diameter is set to 0.3 m. The well is replaced to its equivalent rectangular prism discussed earlier.

8 Because of the high contrast of electrical conductivity between the prism and the background geology,  
9 the high concentration of the electrical current preferentially flows along the surface of the prism and  
10 directly charges HAFZ. We consider that the high-pressure injection of saline fluid creates HAFZ (Kim et  
11 al., 2014). HAFZ is created perpendicular to the horizontal well and 200m away from the vertical well.  
12 Note that this is a relatively shallow hydraulic fracturing model. Depths of fracturing operations range  
13 from 3 to 5 km (Fisher and Warpinski, 2012). Their lateral distance from the vertical well also varies  
14 from 1.6 to 5km. The deeper depth and longer lateral distance mean that anomalous responses to HAFZ  
15 can be significantly smaller than those shown here. Accordingly, they would be vulnerable to cultural  
16 noises. In such cases, one may need to consider downhole based methods presented in Hoversten et al.  
17 (2017). While we are aware of the challenging issues associated with deep fracturing problems, here we  
18 mostly focus on the relatively shallow problem as the basic feasibility study of the top-casing source  
19 electric method.

20 **Figure 6** shows simple four HAFZ models considered in this study. Their dimensions are summarized  
21 in **Table 1**. Note that the fracture propagation is bounded within the overburden and underburden layers  
22 that have higher minimum horizontal stress and/or higher strength than those of the reservoir, propagating  
23 in a horizontal direction. The size and the shape of the HAFZ models above are comparable to those that  
24 can be determined by well-known analytic fracture models such as Khristianovic-Geertsma-de Klerk

1 (KGD) and Perkins-Kern-Nordgen (PKN) fracture (Perkins and Kern, 1961; Geertsma and de Klerk,  
2 1969; Nordgren, 1972; Daneshy, 1973; Gidley et al., 1990) and thus, honor basic geomechanics  
3 associated with fractures. As shown in **Table 1**, we do not consider directly modeling micro-scale fracture  
4 networks. Rather, the thickness of the fracture networks is artificially inflated into 1m thick HAFZ in a  
5 volume-averaged sense as done in Weiss et al. (2015) and Hoversten et al. (2017). The inflation approach  
6 is geophysically reasonable when the low resolution of the electrical method and the distance between  
7 source/receiver and HAFZ are considered.

8 Before we present numerical modeling examples, we briefly discuss a noise floor. In active fracturing  
9 sites and oil fields, the noise floor may vary by several orders of magnitude. For example, Tietze et al.  
10 (2015) report that the noise floor of electric field measurements in a German oil field is about  $10^{-10}$  V/m,  
11 which is subsequently considered a noise floor in Hoversten et al. (2107). It is also reported that the floor  
12 can often be close to  $10^{-7}$  V/m. Therefore, to achieve a desired noise floor in practice, one must consider  
13 stacking data. For example, when the raw noise floor is  $10^{-9}$  to  $10^{-7}$  V/m, 100 to 1,000,000 stacking  
14 operations are required to achieve  $10^{-10}$  V/m noise floor.

15 **Figure 7** shows the electrical field measurements along survey line 1 and 2 over the four HAFZ models.  
16 The top-casing electrical source method clearly distinguishes between the four models. Their electric field  
17 amplitudes are larger than both optimistic and pessimistic noise floors discussed earlier. To highlight the  
18 role of the steel-cased well as a conduit for a high concentration of electric currents that charge HAFZ, we  
19 repeat the same modeling without the casing. **Figure 8** shows that the electrical field measurements over  
20 the background model and the four models are nearly identical. The surface electrical method does not  
21 sense the presence of HAFZ. This modeling shows that steel-cased wells that have been regarded as a  
22 disturbance to electrical and EM geophysics can be beneficial for sensing deep localized targets when the  
23 wells responses can be accurately and efficiently modeled.

1 Next, we examine two factors that directly control the sensitivity of the electrical method to HAFZ. The  
2 first factor is the continuity of the steel cased well. **Figure 9** shows the electric field measurements over  
3 three different continuity conditions: the intact casing, the corroded casing and the broken casing. To  
4 realize a corroded casing condition, we consider a 1m long low conductivity patch ( $5 \cdot 10^3$  S/m) at  $z=500$ m.  
5 When the casing is completely broken, the 1m long patch has the conductivity of the background ( $5 \cdot 10^{-3}$   
6 S/m). As the continuity is deteriorated due to the corrosion, the method still distinguishes between the  
7 four HAFZ models but its sensitivity decreases. The complete break no longer allows the high  
8 concentration of electrical currents to efficiently flow along the casing and charge HAFZ, resulting in the  
9 complete loss of the sensitivity.

10 The conductivity of the background geology also plays an important role in controlling the overall  
11 sensitivity of the method. **Figure 10** shows the electric field measurement along survey line 1 with three  
12 different background conductivities ranging from  $5 \cdot 10^{-2}$  S/m to  $5 \cdot 10^{-1}$  S/m. As the background geology  
13 becomes more conductive, the sensitivity sharply decreases. The loss of the sensitivity is explained by the  
14 fact that in more conductive background, casing tends to leak more currents horizontally and limits the  
15 flow of the currents to HAFZ. In general, the top-casing electrical source method may not work well in  
16 highly conductive earth environments. However, we have found that the presence of oil-based mud has  
17 potential to improve the sensitivity of the top-casing electric source method even in a conductive  
18 environment, because the mud is highly resistive up to 1,000 Ohm-m and reduces leaking current from  
19 the well (Jannin et al., 2018). To examine the effect of the oil-based mud on the sensitivity, we assume  
20 that the L-shaped well (**Figure 5**) is coated with 0.2m thick, 100 Ohm-m oil-based mud and compute the  
21 surface electric field responses to the fractures in two conductive ( $5 \cdot 10^{-2}$  and  $5 \cdot 10^{-1}$  S/m) background  
22 models (**Figure 11**). The comparison of **Figures 10** and **11** shows that the presence of thin oil-based mud  
23 coating increases the sensitivity of the method by about 80%, demonstrating the potential benefit of oil-  
24 based mud for the top-casing source method for detecting deep HAFZ in a conductive environment.

## 1 INVERSE SENSITIVITY OF TOP-CASING ELECTRIC SOURCE METHOD TO HAFZ

2 In this section, we examine the imaging sensitivity to the four HAFZ models (**Figure 6** and **Table 1**) as  
3 the final step of proof-of-concept studies for the top-casing electrical source method. To ensure the  
4 detection sensitivity to HAFZ, we assume that the background geology is resistive enough (i.e.  $5 \cdot 10^{-3}$   
5 S/m) such that the electrical currents can flow through the casing without significant leakage. The  
6 Permian Basin and the Marcellus shale can be considered such resistive. We also assume that the cased  
7 well is homogeneous and continuous. In addition, we adapt two extra assumptions from Hoversten et al.  
8 (2017) that (1) electric field measurements are contaminated with 1% error of their amplitudes and (2)  
9 electric field noise floor is  $10^{-10}$  V/m. The four assumptions might not always be satisfied in practice.  
10 However, the consideration about their potential influences is avoided in this study to focus on the basic  
11 imaging capabilities of the top-casing electrical methods for HAFZ.

12 **Figure 12** summarizes the imaging experiment over HAFZ model 1. The starting model is a  $5 \cdot 10^{-3}$  S/m  
13 homogeneous half-space. An imaging domain covers  $0 \leq x \leq 400$ ,  $-1000 \leq y \leq 1000$  and  
14  $1000 \leq z \leq 2000$ m. In other words, we assume that HAFZ resides inside the volume defined by the  
15 imaging domain. The L-BFGS-based imaging algorithm implemented here work well and converges after  
16 15 iterations. The inversion is completed in 3 hours on 3.40GHz Intel Skylake processor with 64 GB  
17 memory. After the convergence, both observed and predicted data show good agreements. The inversion  
18 reasonably recovers the overall geometry of the HAFZ model 1 on the  $yz$  plane at  $x=200$ m (**Figure 12a**)  
19 although some scattered artifacts are seen on the  $xz$  plane at  $y=0$ m (**Figure 12b**).

20 Note that the boundaries of the recovered HAFZ are not smooth but somewhat irregular. This is  
21 because we use a relatively small regularization parameter in our inversion. A proper small regularization  
22 parameter is empirically determined via trial errors. It is our experience that a traditional cooling method  
23 with a large starting regularization parameter often smooths out a thin HAFZ structure in early inversion



1 stages and fails to recover the fracture geometry in late stages with a small parameter. Accordingly,  
2 choosing a small starting regularization parameter is our practical choice for imaging thin HAFZ when a  
3 smooth background conductivity model is determined by other geophysical methods (e.g. Um et al.,  
4 2014).

5 In the experiment above, our imaging domain does not cover the entire modeling volume. We have  
6 found out that such a large imaging domain often leads to non-geological imaging results (e.g. highly  
7 scattered conductive structures). Instead, our imaging domain covers the horizontal well area with  
8 sufficient room for fracture developments in both lateral and vertical direction. While our proof-of-  
9 concept studies assume that the HAFZ is perpendicular to the well, realistic scenarios may involve that its  
10 geometry changes over time. Therefore, 400-by-2000-by1000m volume of the imaging domain would be  
11 reasonable. However, knowledge of both the fluid injection location and the amount of the injected fluid  
12 helps us to estimate a possible maximum volume of the imaging domain (Hoversten et al., 2017).  
13 Coupled flow and geomechanics simulation for various scenarios with different geological media (Kim  
14 and Moridis, 2013) can further assist refining the imaging domain size.

15 MEQ analysis can also roughly tell us about the locations of fracturing events, helping us better define a  
16 volume of the imaging domain. Therefore, it is worth to perform imaging experiments with an MEQ-  
17 guided imaging domain. For example, we assume that by having MEQ analysis, we can reduce  
18  $0 \leq x \leq 400$  of the imaging domain to  $175 \leq x \leq 225$ m where we have an injection point at ( $x=200$ m,  $y=0$ m  
19 and  $z=1600$ m). The assumption is also reasonable from geomechanical perspectives because the domain  
20 size of 50m in the  $x$  direction would be sufficiently large such that HAFZ can contain both main fracture  
21 networks and small micro-fractures/fissures that can induce substantial leakage of injection fluid (Fisher  
22 and Warpinski, 2012). The other dimensions of the imaging domain keep the same as those used in  
23 **Figure 12.**

1 **Figure 13** shows the imaging experiments for model 1 with the imaging domain constrained in the  $x$   
2 direction. Although the thickness of HAFZ model 1 is still not clearly resolved but blurred, the width and  
3 the height of model 1 are slightly better resolved. The use of the tight imaging domain also prevents  
4 unrealistic scattered conductive structures on the  $xz$  plane at  $y=0\text{m}$  shown in **Figure 12b**. **Figures 14-16**  
5 show the imaging experiments for the remaining three HAFZ models with the same constrained imaging  
6 domain. **Figures 13-16** clearly show that the casing-top electrical method can effectively delineate  
7 systematical changes in the width and the height of HAFZ although it is still daunting to resolve the  
8 thickness even in the imaging domain constrained in its direction.

9 Our last inversion experiment examines the effects of a higher noise level on the imaging sensitivity. To  
10 do this, the noise level for model 1 increases from 1 to 5 %. All other inverse modeling parameters and  
11 the volume of the imaging domain keep the same as those used in **Figure 13**. **Figure 17** summarizes the  
12 imaging experiment with the high noise level. The inversion algorithm performs well and its convergence  
13 is similar to the previous examples. Compared with the inversion result with 1% noise (**Figure 13**), the  
14 height of HAFZ is reasonably recovered, but the accuracy of the width is deteriorated. This inversion  
15 example illustrates the importance of data quality for accurately resolving the detailed geometry of  
16 HAFZ.

## 17 **CONCLUSION**

18 We have presented advanced 3D electrical resistivity modeling and imaging algorithms that utilize  
19 heterogeneous types of meshes. The coarse rectangular FD meshes are used in the imaging domain to  
20 facilitate visualization and analysis of imaging results, whereas the tetrahedral FE simulation meshes are  
21 used for efficiently and accurately discretizing a multi-scale earth model. Linear mapping operators based  
22 on volume-averaging provides a robust link between the two difference mesh topologies. The algorithms  
23 are well suited to modeling and inverting electric field measurements in the presence of a steel-cased well.

1 We have shown that a steel-cased well can be replaced by a prism. This replacement reduces the  
2 computational cost without deteriorating the solution accuracy, making it possible to rapidly simulate  
3 electric field responses over a 3D earth model in the presence of a steel-cased well.

4 We have shown that the top-casing electrical method is sensitive to and can delineate a localized HAFZ  
5 in a shallow depth. The primary advantage of the proposed method is the fact that the method employs  
6 surface sources and receivers and thus does not require borehole occupancy and interruption to the normal  
7 operation of the wells. As a result, its data acquisition can be cheaper and less cumbersome. We have  
8 numerically shown that the top-casing electric source method has potential to image HAFZ. The imaging  
9 results can be improved if the imaging domain is constrained.

10 To evaluate the proof of concept for the top-casing electrical method, our feasibility studies focused on  
11 fairly simple 3D HAFZ models. Several assumptions were also made to render our studies simple. For  
12 example, HAFZ is relatively shallow. The properties of the background geology and the steel-cased well  
13 were assumed known. However, in practice, it may not be always straightforward to characterize a deep  
14 localized HAFZ. A baseline resistivity model should be determined before hydraulic fracturing  
15 operations. The casing properties are also often unknown and may need to be determined by inversion.  
16 Accordingly, we expect that there are still challenges to accurately characterize deep HAFZ in practice.  
17 However, the feasibility studies presented here is encouraging. When the top-casing source method is  
18 considered for imaging HAFZ, the challenges described above will be important research topics.

## 19 **ACKNOWLEDGEMENT**

20

1 **APPENDIX. MAPPING MATRICES  $\mathbf{M}_{\text{FE2FD}}$  and  $\mathbf{M}_{\text{FD2FE}}$**

2 The mapping processes from FD to FE meshes are casted into

$$\boldsymbol{\sigma}^{FE} = \mathbf{M}_{\text{FD2FE}} \boldsymbol{\sigma}^{FD}; \quad (\text{A1})$$

$$\mathbf{M}_{\text{FD2FE}ij} = \frac{1}{v_i^{FE}} \times (v_i^{FE} \cap v_j^{FD}) \quad (\text{A2})$$

(i,j) element of .

3  $N_{\text{FE}}$ -by- $N_{\text{FD}}$  matrix  $\mathbf{M}_{\text{FD2FE}}$  is a mapping operator from FD to FE meshes. Vectors  $\boldsymbol{\sigma}^{FE}$  and  $\boldsymbol{\sigma}^{FD}$  contain

4 conductivity attributes of the FE and FD models, respectively.  $v_i^{FE}$  and  $v_j^{FD}$  are the volume of the  $i^{\text{th}}$  FE

5 element and the  $j^{\text{th}}$  FD element, respectively. The intersection operator  $\cap$  computes the overlapping

6 volume of the FE and FD cell if they intersect.

7  $N_{\text{FD}}$ -by- $N_{\text{FE}}$  matrix  $\mathbf{M}_{\text{FE2FD}}$  is defined in the reverse way as shown below.

$$\boldsymbol{\sigma}^{FD} = \mathbf{M}_{\text{FE2FD}} \boldsymbol{\sigma}^{FE}; \quad (\text{A3})$$

$$\mathbf{M}_{\text{FE2FD}ij} = \frac{1}{v_i^{FD}} \times (v_i^{FD} \cap v_j^{FE}) \quad (\text{A4})$$

(i,j) element of .

8

## 1 REFERENCES

- 2 Jannin, G., J. Chen, L. DePavia, L. Sun and M. Schwart, 2017, Deep electrode: A game-changing  
3 technology for electromagnetic (EM) telemetry, Annual International Meeting, SEG, Expanded Abstracts,  
4 1059-1062.
- 5 Commer, M., G. M. Hoversten, and E. S. Um, 2015, Transient-electromagnetic finite-difference time-  
6 domain earth modeling over steel infrastructure, *Geophysics*, **80**, E147-E162.
- 7 Commer, M., and G. A. Newman, 2008, New advances in three-dimensional controlled-source  
8 electromagnetic inversion, *Geophysical Journal International*, **172**, 513-535.
- 9 Commer, M. and G. A. Newman, 2004, A parallel finite-difference approach for 3D transient  
10 electromagnetic modeling with galvanic sources, *Geophysics* **69**, 1192-1202.
- 11 Cuevas, N., 2014, Analytical solutions of EM fields due to a dipole source inside an infinite casing,  
12 *Geophysics*, 79, E231-241.
- 13 Daneshy, A.A., 1973. On the Design of Vertical Hydraulic Fractures. *SPE Journal of Petroleum*  
14 *Technology* **25**, 83-97.
- 15 Davis, T.A., 2006, Direct methods for sparse linear systems, *Society for Industrial and Applied*  
16 *Mathematics*.
- 17 Egbert, G. D., and A. Kelbert, 2012, Computational recipes for electromagnetic inverse  
18 problems, *Geophysical Journal International*, **189**, 251-267.
- 19 Fisher, K., and N. Warpinski, 2012, Hydraulic fracture-height growth: real data. *SPE Prod. Oper.* **27**, 8-  
20 19

- 1 Grayver, A. V., 2015, Parallel three-dimensional magnetotelluric inversion using adaptive finite-  
2 element method. Part I: theory and synthetic study, *Geophysical Journal International*, **202**, 584-603.
- 3 Geertsma, J., and F. de Klerk, 1969. A Rapid Method of Predicting Width and Extent of Hydraulic  
4 Induced Fractures. *J Pet Technol* **2**, 1571-1581, SPE-2458-PA.
- 5 Gidley, J.L., S. A. Holditch, D. E. Nierode, W. Ralph, and R. W. Veatch, 1990, Recent advances in  
6 hydraulic fracturing. *SPE Monograph Series Vol. 12*.
- 7 Hoversten, G. M., Commer, M., E. Haber, and C. Schwarzbach, 2015, Hydro-frac monitoring using  
8 ground time-domain electromagnetics, *Geophysical Prospecting*, **63**, 1508-1526.
- 9 Hoversten, M., C. Schawrzbach, E. Haber, P. Belliveau and R. Shekhtman, 2017, Borehole to surface  
10 electromagnetic monitoring of hydraulic fractures, 6<sup>th</sup> International Symposium on Three-Dimensional  
11 Electromagnetics, Berkeley, California, USA.
- 12 Jin, J.M., 2015, *The finite element method in electromagnetics*, 3<sup>rd</sup> edition, John Wiley & Sons.
- 13 Johnston, R. and J. Shralow, 2011, Ambiguity in microseismic monitoring. Annual International  
14 Meeting, SEG, Expanded Abstracts, 1514-1518.
- 15 Kim, J. and G. J. Moridis, 2013, Development of the T+ M coupled flow–geomechanical simulator to  
16 describe fracture propagation and coupled flow–thermal–geomechanical processes in tight/shale gas  
17 systems. *Computers & Geosciences*, **60**, 184-198.
- 18 Kim, J., E. S. Um, and G. J. Moridis, 2014, Fracture propagation, fluid flow, and geomechanics of  
19 water-based hydraulic fracturing in shale gas systems and electromagnetic geophysical monitoring of  
20 fluid migration, *SPE Hydraulic Fracturing Technology Conference*, Society of Petroleum Engineers.

1 Marsala, A.F., A. D. Hibbs, and H. F. Morrison, 2014, December. Evaluation of Borehole Casing  
2 Sources for Electromagnetic Imaging of Deep Formations, International Petroleum Technology  
3 Conference.

4 Moridis, G.J. and C. M. Oldenburg, 2001, Process for guidance, containment, treatment, and imaging in  
5 a subsurface environment utilizing ferro-fluids (No. US 6250848), Lawrence Berkeley National  
6 Laboratory (LBNL), Berkeley, CA.

7 Newman, G.A. and D. L. Alumbaugh, 2000. Three-dimensional magnetotelluric inversion using non-  
8 linear conjugate gradients. *Geophysical journal international*, **140**, 410-424.

9 Nieuwemhuis, G., D. Yang, K. MacLennan, D. Oldenburg, M. Wilt and V. Ramadoss, 2015, Electrical  
10 imaging using a well casing as an antenna: a case study from a CO<sub>2</sub> sequestration site in Montana,  
11 American Geophysical Union Meeting.

12 Nocedal, J., and S. Wright, 2006, Numerical optimization, Springer Science & Business Media.

13 Nordgren, R.P., 1972. Propagation of a Vertical Hydraulic Fracture. *SPE J.* 12 (4): 306–314. SPE-3009-  
14 PA.

15 Patzer, C., K. Tietze, and O. Ritter, 2017, Steel-cased wells in 3-D controlled source EM  
16 modelling. *Geophysical Journal International*, **209**, 813-826.

17 Perkins, T.K., and L. R. Kern, 1961. Widths of Hydraulic Fractures. *J Pet Technol*, **13**, 937–949.

18 Puzyrev, V., E. Vilamajo, P. Queralt, J. Ledo, and A. Marcuello, 2016, Three-Dimensional Modeling of  
19 the Casing Effect in Onshore Controlled-Source Electromagnetic Surveys, *Surveys in Geophysics*, **38**,  
20 527-545.

- 1 Rahmani, A.R., A. E. Athey, J. Chen, and M. J. Wilt, 2014, Sensitivity of dipole magnetic tomography  
2 to magnetic nanoparticle injectates, *Journal of Applied Geophysics*, **103**, 199-214.
- 3 Schenkel, C.J. and H. F. Morrison, 1994. Electrical resistivity measurement through metal  
4 casing. *Geophysics*, **59**, 1072-1082.
- 5 Si, H., 2015, TetGen, a Delaunay-based quality tetrahedral mesh generator. *ACM Transactions on*  
6 *Mathematical Software (TOMS)*, **4**, 11.
- 7 Tietze, K., O. Ritter, and P. Veecken, 2015, Controlled-source electromagnetic monitoring of reservoir  
8 oil saturation using a novel borehole-to-surface configuration, *Geophysical Prospecting*, **63**, 1468-1490.
- 9 Um, E. S., J. M. Harris, and D. L. Alumbaugh, 2010. 3D time-domain simulation of electromagnetic  
10 diffusion phenomena: A finite-element electric-field approach. *Geophysics*, **75**, F115-F126.
- 11 Um, E. S., M. Commer, and G. Newman. 2014, A strategy for coupled 3D imaging of large-scale  
12 seismic and electromagnetic data sets: Application to subsalt imaging, *Geophysics* **79**, ID1-ID13.
- 13 Um, E. S., M. Commer, G. A. Newman, and G. M. Hoversten, 2015. Finite element modelling of  
14 transient electromagnetic fields near steel-cased wells. *Geophysical Journal International*, **202**, 901-913.
- 15 Um, E. S., S. Kim and H. Fu, 2017, A tetrahedral mesh generation approach for 3D marine controlled-  
16 source electromagnetic modeling, *Computer and Geosciences*, **100**, 1-9.
- 17 Vermylen, J.P. and M.D. Zoback. 2011. Hydraulic fracturing, microseismic magnitudes, and stress  
18 evolution in the Barnett Shale, Texas, USA. *SPE Hydraulic Fracturing Technology Conference*, The  
19 woodland, TX, 24 – 26 Jan. 2011.
- 20 Warpinski, N.R., R.C. Kramm, J.R. Heinze, and C.K. Waltman. 2005. Comparison of single- and dual-  
21 array microseismic mapping techniques in the Barnett shale. *SPE ATCE*, Dallas, TX, Oct. 9 – 12 2005.



- 1 Weiss, C. J., D. F. Aldridge, H. A. Knox, K. A. Schramm, and L. C. Bartel, 2016, The direct-current  
2 response of electrically conducting fractures excited by a grounded current source. *Geophysics*, **81**, E201-  
3 E210.
- 4 Weiss, C., 2017, Finite-element analysis for model parameters distributed on a hierarchy of geometric  
5 simplices, *Geophysics*, **82**, no. 4, E155-E167.
- 6 Yang, D., D. Oldenburg, and E. Haber, 2014, 3-D inversion of airborne electromagnetic data  
7 parallelized and accelerated by local mesh and adaptive soundings: *Geophysical Journal International*,  
8 **196**, 1942-1507.
- 9 Yang, D., and D. Oldenburg, 2016, Survey decomposition: A scalable framework for 3D controlled-  
10 source electromagnetic inversion: *Geophysics*, **81**, E69-E87.
- 11 Zoback M.D. 2007 Reservoir geomechanics. Cambridge, Cambridge university press.
- 12 Zoback, M., Kitasei, S., and Copithorne, B. 2010 Addressing the environmental risks from shale gas  
13 development. World Watch Institute Briefing Paper 1, World watch Institute (Washington DC)

## 1 FIGURE CAPTIONS

2 **Figure 1.** (a) 200m long hollow steel-cased well model. The air, the earth and the casing are set to  $3 \cdot 10^{-7}$ ,  $3 \cdot 10^{-2}$  and  $10^6$  (S/m), respectively. (b) Its corresponding solid rectangular prism model.

4 **Figure 2.** Comparison of surface  $+x$ -oriented electric field responses to the two models (**Figure 1**).

5 **Figure 3.**  $XY$  cross-sectional views of 3D FD models with a conductivity color bar (log scale). (a) A  
6 1km long vertical hollow steel-cased well. (b) A solid cylinder that has the same outer diameter of the  
7 hollow steel-cased well. (c) A rectangular prism of which its side length is equal to the diameter of the  
8 hollow steel-cased well. The earth and the casing are set to  $3.33 \cdot 10^{-2}$  and  $5 \cdot 10^6$  S/m, respectively. The  
9 cylinder and prism are set to  $1.73 \cdot 10^6$  and  $1.36 \cdot 10^6$  S/m, respectively.  $R_{in}$  and  $R_{out}$  represent the inner and  
10 outer radius of the casing, and  $W$  the width of the rectangular prism.

11 **Figure 4.** Comparison of DC responses to the true and approximate casing models shown in **Figure 3**.  
12 (a) Surface  $+x$ -oriented electric field responses. (b) Relative differences of the approximate model  
13 responses with respect to the hollow cased well model response.

14 **Figure 5.** A top-casing electric source configuration for detecting HAFZ at  $z=1.6$  km and  $x=200$ m.  $X$ -  
15 oriented and  $y$ -oriented electric fields are measured along survey line 1 and 2, respectively.

16 **Figure 6.** The four hydraulically active fractured zone models. The  $yz$  cross-sectional view at  $x=200$ m  
17 (a) Model 1. (b) Model 2. (c) Model 3. (d) Model 4.

18 **Figure 7.** Electric field measurements along (a) survey line 1 and (b) survey line 2 and their relative  
19 difference with respect to the 0.005 S/m (200 Ohm-m) background response.

20 **Figure 8.** Electric field measurements without the steel-cased well along (a) survey line 1 and (b)  
21 survey line 2 and their relative difference with respect to the background response.

1 **Figure 9.** Electric field measurements along +x axis (survey line 1) with partially and fully damaged  
2 cased wells. (a) Intact ( $5 \cdot 10^6$  S/m) casing (**Figure 5a**). (b) The corroded ( $5 \cdot 10^3$  S/m) casing at  $z=500$ m. (c)  
3 The completely broken casing at  $z=500$ m.

4 **Figure 10.** Electric field measurements along +x axis (survey line 1) with different background  
5 conductivity values. (a) Background conductivity= $5 \cdot 10^{-2}$  S/m. (b) Background conductivity= $5 \cdot 10^{-1}$  S/m.

6 **Figure 11.** Electric field measurements along +x axis (survey line 1) with different background  
7 conductivity values. (a) Background conductivity= $5 \cdot 10^{-2}$  S/m. (b) Background conductivity= $5 \cdot 10^{-1}$  S/m.  
8 The cased well is coated with 0.2m thick  $10^{-2}$  S/m oil-based mud.

9 **Figure 12.** Inversion for model 1. (a) YZ cross-sectional view at  $x=200$ m. (b) XZ cross-sectional view at  
10  $y=0$ m. (c) Data plots along line 1 before and after the inversion. (d) Data plots along line 2 before and  
11 after the inversion. (e) Misfit as a function of inversion iteration. The white boxes in (a) and (b) indicate  
12 the true boundaries of model 1.

13 **Figure 13.** Inversion for model 1 with the imaging domain constrained in the x-direction. (a) YZ cross-  
14 sectional view at  $x=200$ m. (b) XZ cross-sectional view at  $y=0$ m. (c) Data plots along line 1 before and  
15 after the inversion. (d) Data plots along line 2 before and after the inversion. (e) Misfit as a function of  
16 inversion iteration. The white boxes in (a) and (b) indicate the true boundaries of model 1.

17 **Figure 14.** Inversion for model 2 with the imaging domain constrained in the x-direction. (a) YZ cross-  
18 sectional view at  $x=200$ m. (b) XZ cross-sectional view at  $y=0$ m. (c) Data plots along line 1 before and  
19 after the inversion. (d) Data plots along line 2 before and after the inversion. (e) Misfit as a function of  
20 inversion iteration. The white boxes in (a) and (b) indicate the true boundaries of model 2.

21 **Figure 15.** Inversion for model 3 with the imaging domain constrained in the x-direction. (a) YZ cross-  
22 sectional view at  $x=200$ m. (b) XZ cross-sectional view at  $y=0$ m. (c) Data plots along line 1 before and

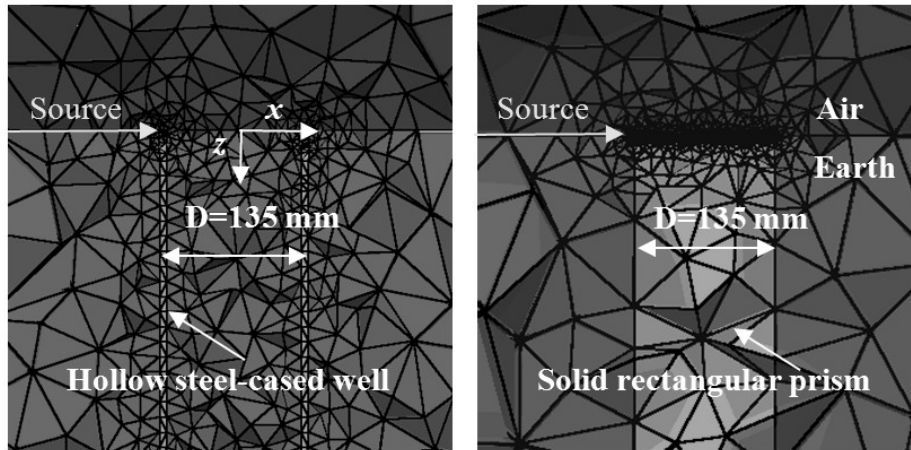
1 after the inversion. (d) Data plots along line 2 before and after the inversion. (e) Misfit as a function of  
2 inversion iteration. The white boxes in (a) and (b) indicate the true boundaries of model 3.

3 **Figure 16.** Inversion for model 4 with the imaging domain constrained in the x-direction.. (a) YZ cross-  
4 sectional view at x=200m. (b) XZ cross-sectional view at y=0m. (c) Data plots along line 1 before and  
5 after the inversion. (d) Data plots along line 2 before and after the inversion. (e) Misfit as a function of  
6 inversion iteration. The white boxes in (a) and (b) indicate the true boundaries of model 4.

7 **Figure 17.** Inversion for model 1 with 5% noise level. (a) YZ cross-sectional view at x=200m. (b) XZ  
8 cross-sectional view at y=0m. (c) Data plots along line 1 before and after the inversion. (d) Data plots  
9 along line 2 before and after the inversion. (e) Misfit as a function of inversion iteration.

10

1 FIGURES



2

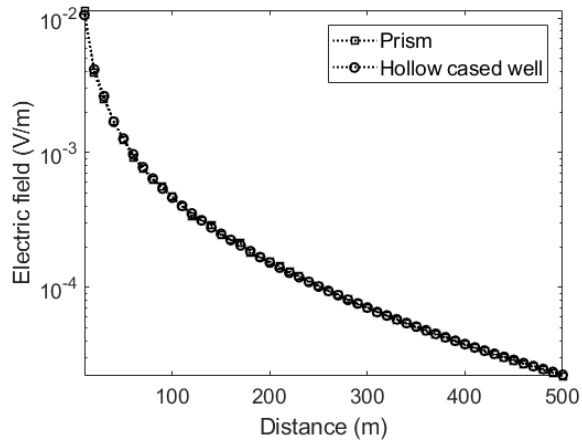
3

(a)

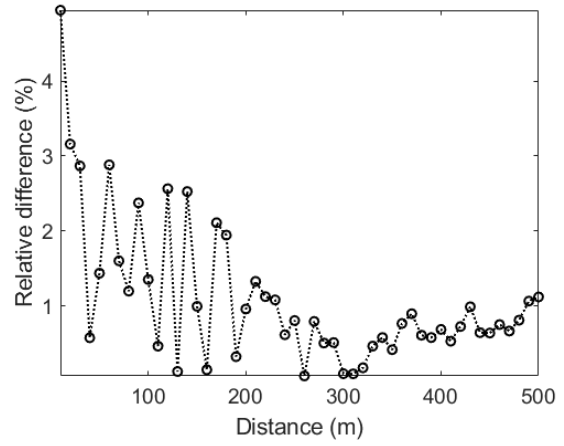
(b)

4 **Figure 1.** (a) 200m long hollow steel-cased well model. The air, the earth and the casing are set to  $3 \cdot 10^{-7}$ ,  
5  $3 \cdot 10^{-2}$  and  $10^6$  (S/m), respectively. (b) Its corresponding solid rectangular prism model.

6



(a)



(b)

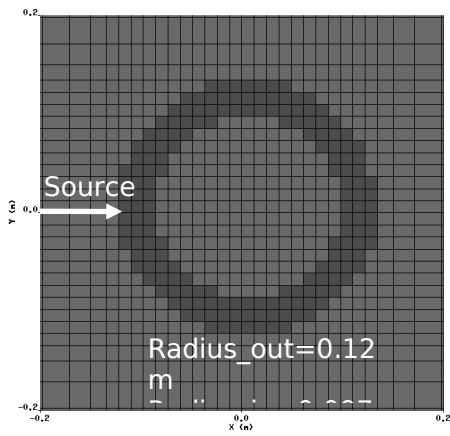
**Figure 2.** Comparison of surface  $+x$ -oriented electric field responses to the two models (**Figure 1**).

1

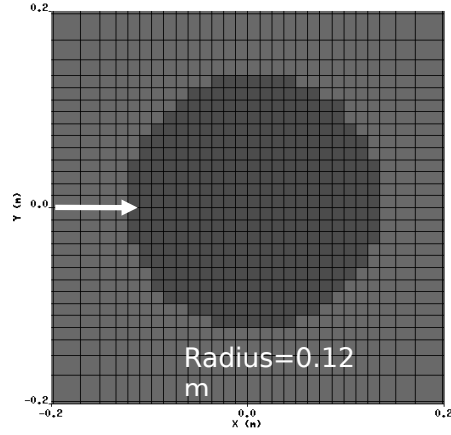
2

3

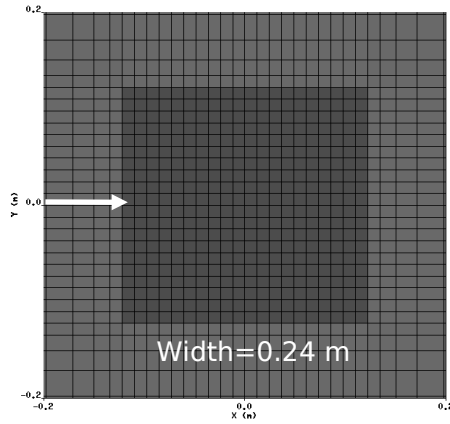
4



(a)



(b)



(c)

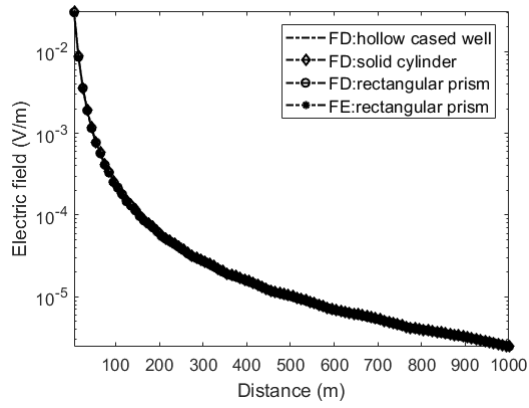
1  
2

3  
4

5 **Figure 3.** *XY* cross-sectional views of 3D FD models with a conductivity color bar (log scale). (a) A  
6 1km long vertical hollow steel-cased well. (b) A solid cylinder that has the same outer diameter of the  
7 hollow steel-cased well. (c) A rectangular prism of which its side length is equal to the diameter of the  
8 hollow steel-cased well. The earth and the casing are set to  $3.33 \cdot 10^{-2}$  and  $5 \cdot 10^6$  S/m, respectively. The  
9 cylinder and prism are set to  $1.73 \cdot 10^6$  and  $1.36 \cdot 10^6$  S/m, respectively.  $R_{in}$  and  $R_{out}$  represent the inner and  
10 outer radius of the casing, and  $W$  the width of the rectangular prism.

11

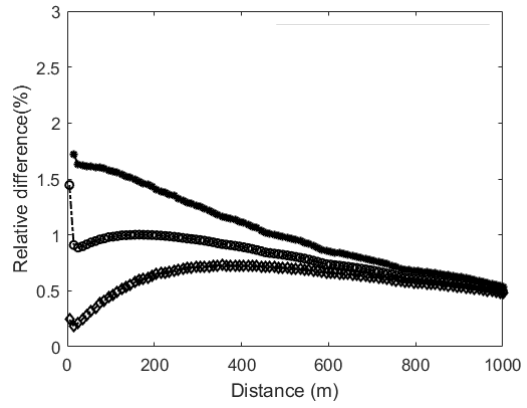
1



2

3

(a)

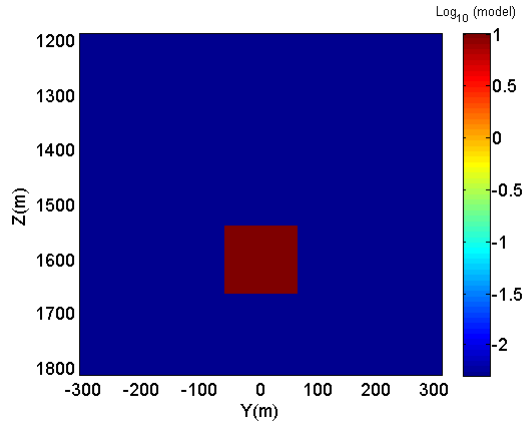


(b)

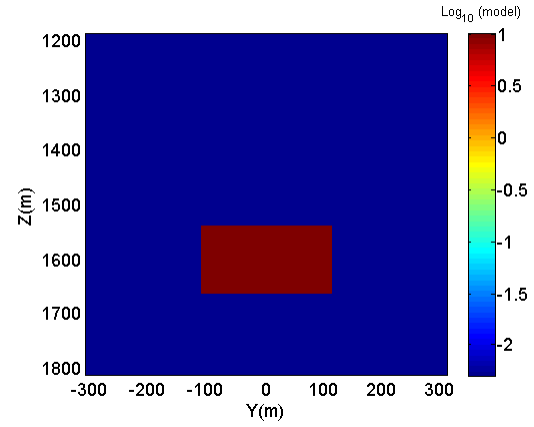
4 **Figure 4.** Comparison of DC responses to the true and approximate casing models shown in **Figure 3.** (a)  
5 Surface  $+x$ -oriented electric field responses. (b) Relative differences of the approximate model responses  
6 with respect to the hollow cased well model response.



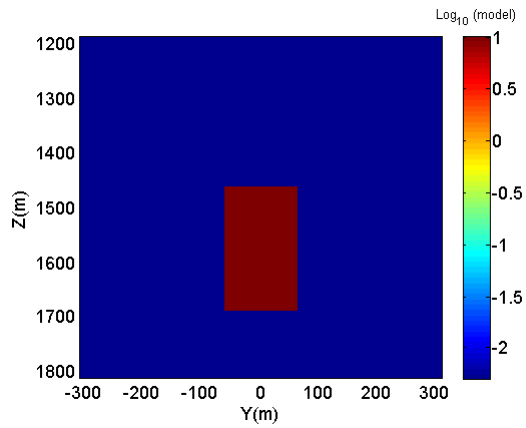




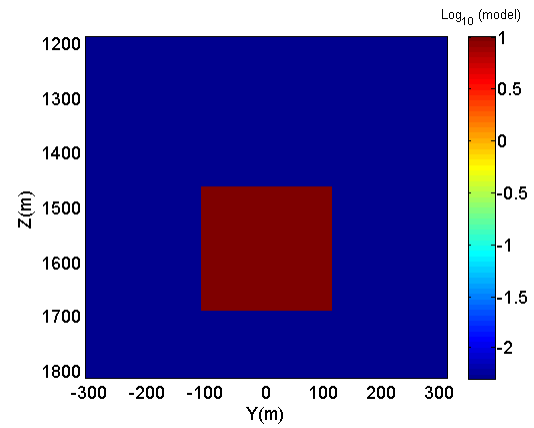
(a)



(b)



(c)



(d)

1

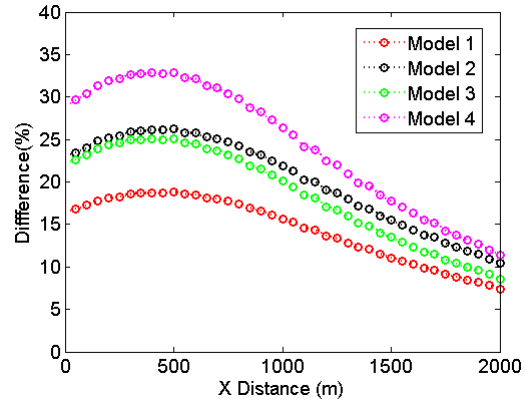
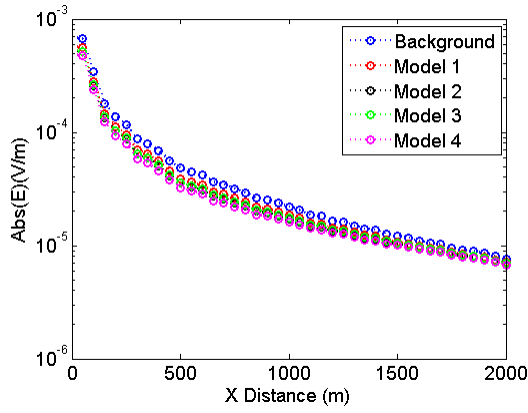
2

3

4

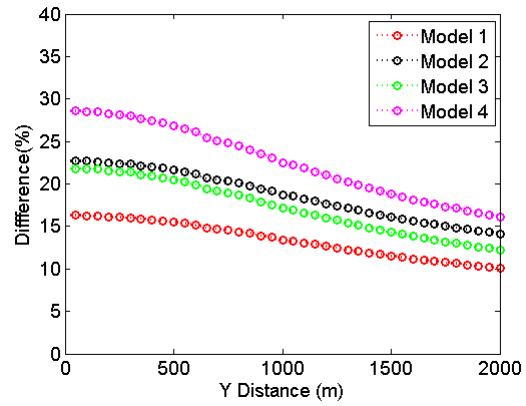
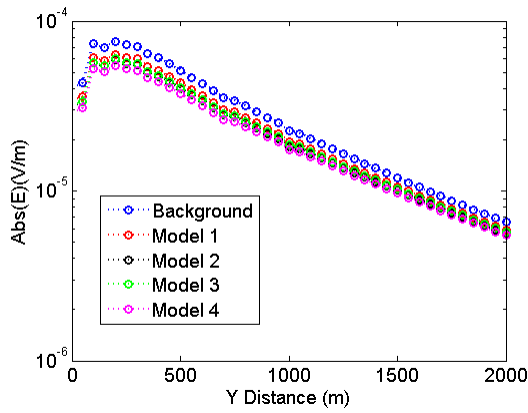
5 **Figure 6.** The four hydraulically active fractured zone models. The  $yz$  cross-sectional view at  $x=200\text{m}$  (a)

6 Model 1. (b) Model 2. (c) Model 3. (d) Model 4.



1  
2

(a)

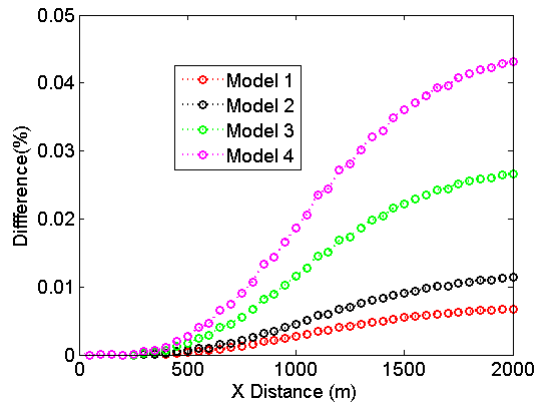
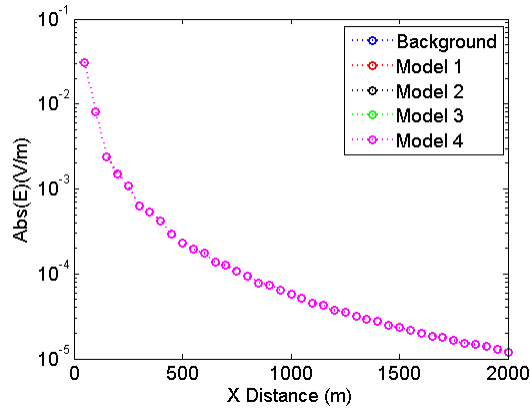


3  
4

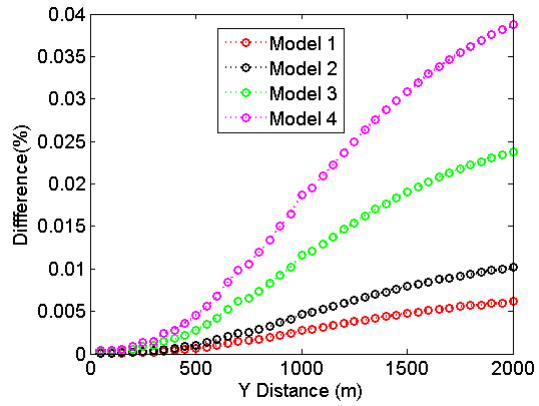
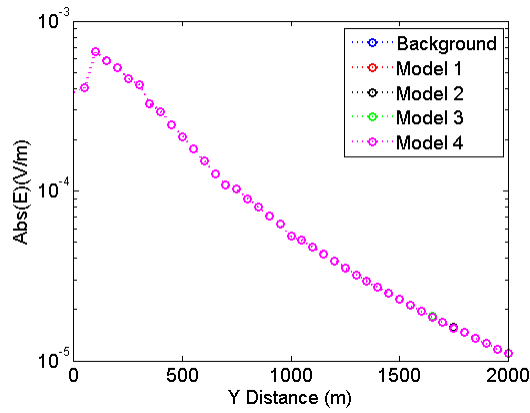
(b)

5 **Figure 7.** Electric field measurements along (a) survey line 1 and (b) survey line 2 and their relative  
6 difference with respect to the 0.005 S/m (200 Ohm-m) background response.

7

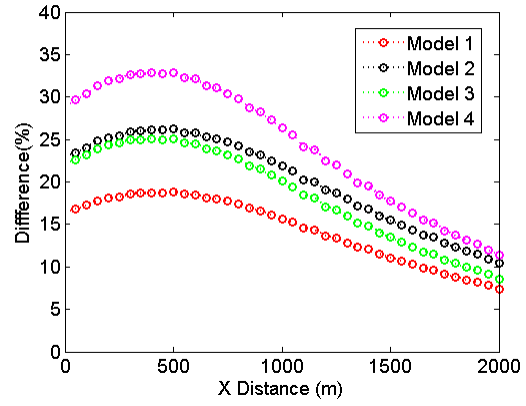
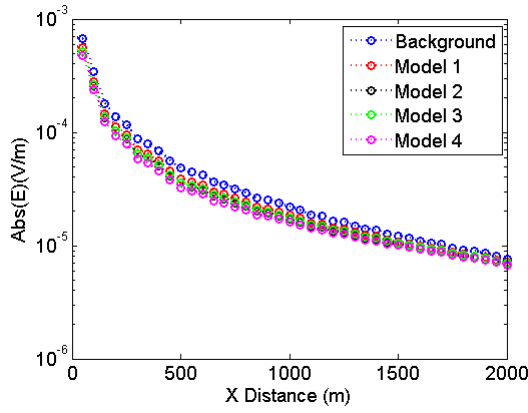


(a)

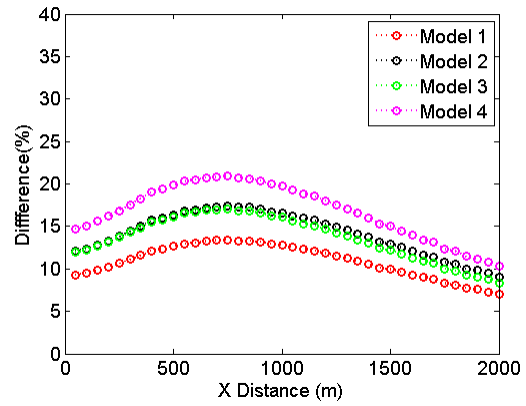
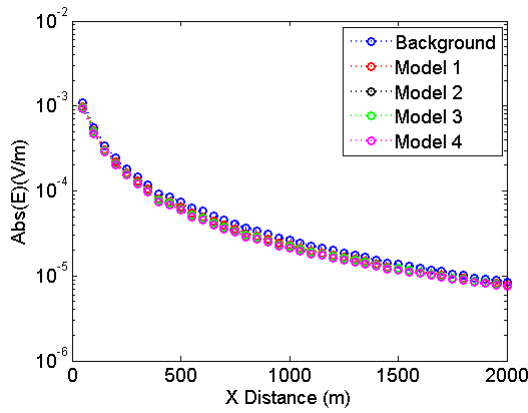


(b)

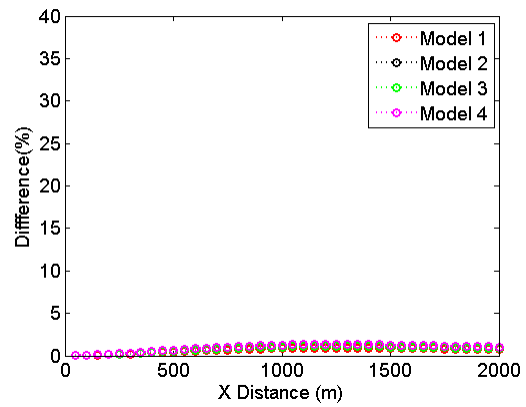
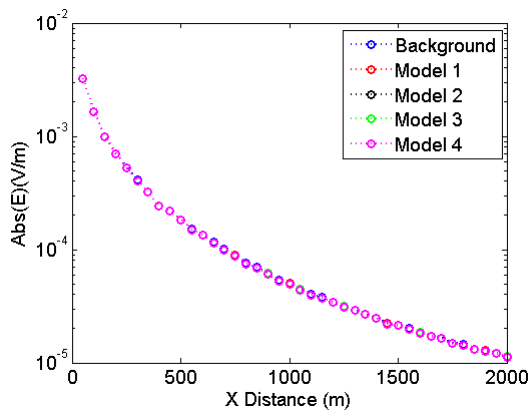
**Figure 8.** Electric field measurements without the steel-cased well along (a) survey line 1 and (b) survey line 2 and their relative difference with respect to the background response.



(a)

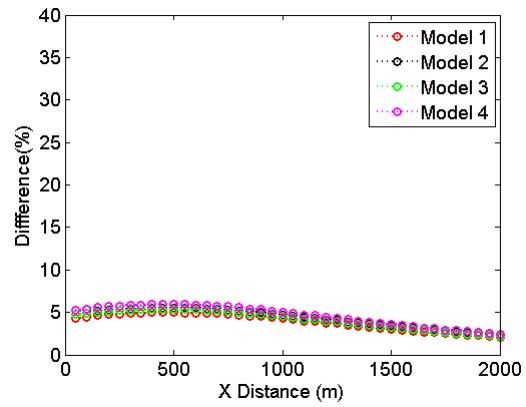
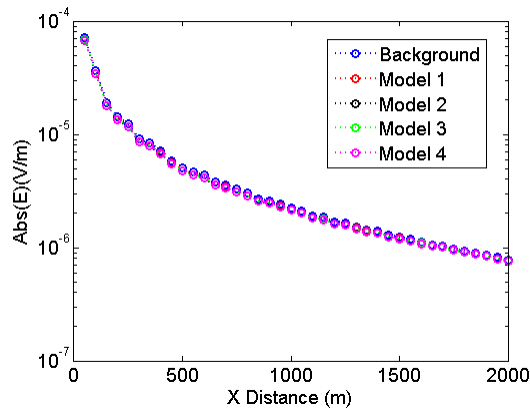


(b)

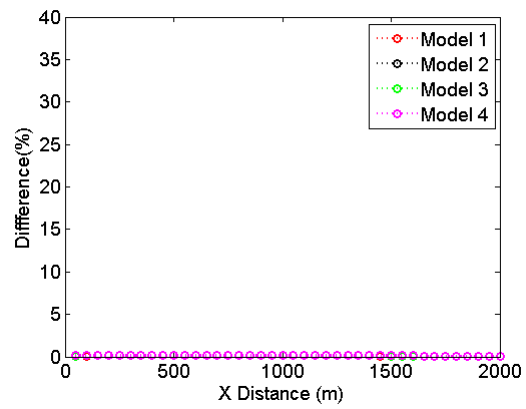
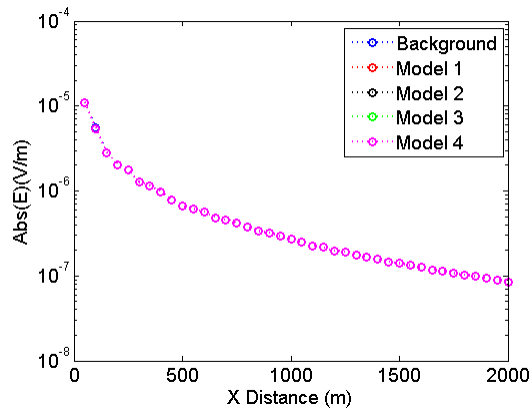


(c)

**Figure 9.** Electric field measurements along +x axis (survey line 1) with partially and fully damaged cased wells. (a) Intact ( $5 \cdot 10^6$  S/m) casing (**Figure 5a**). (b) The corroded ( $5 \cdot 10^3$  S/m) casing at  $z=500$ m. (c) The completely broken casing at  $z=500$ m.

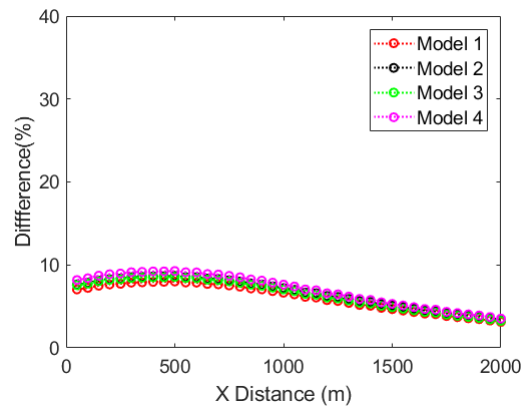
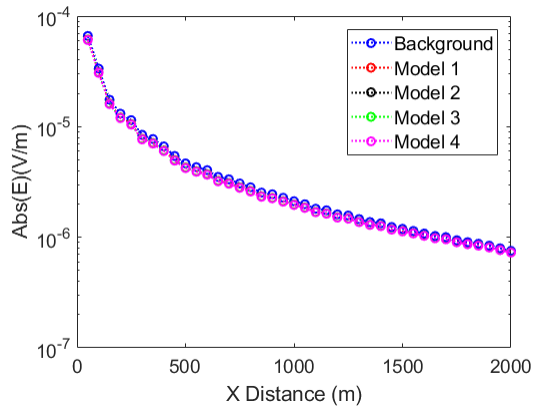


(a)

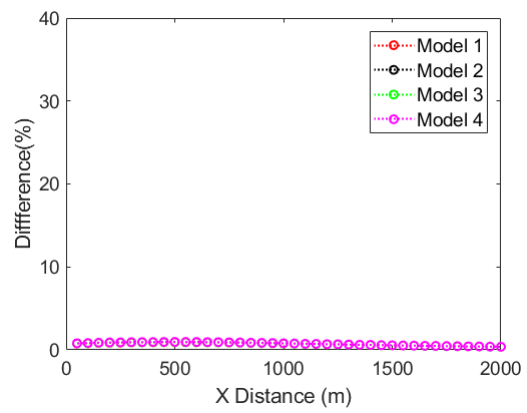
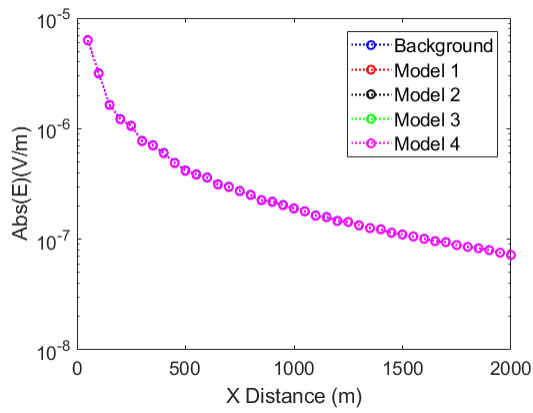


(b)

**Figure 10.** Electric field measurements along +x axis (survey line 1) with different background conductivity values. (a) Background conductivity= $5 \cdot 10^{-2}$  S/m. (b) Background conductivity= $5 \cdot 10^{-1}$  S/m.

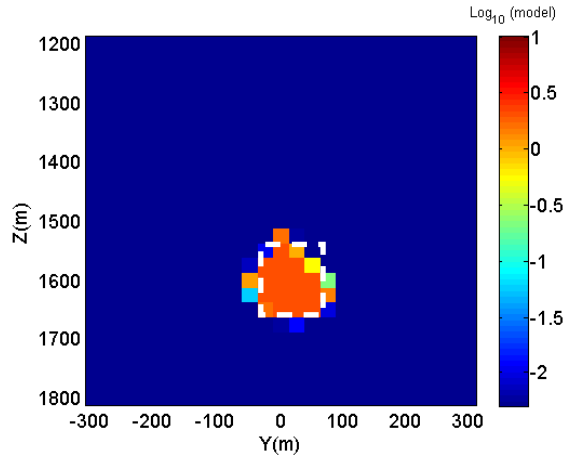


(a)

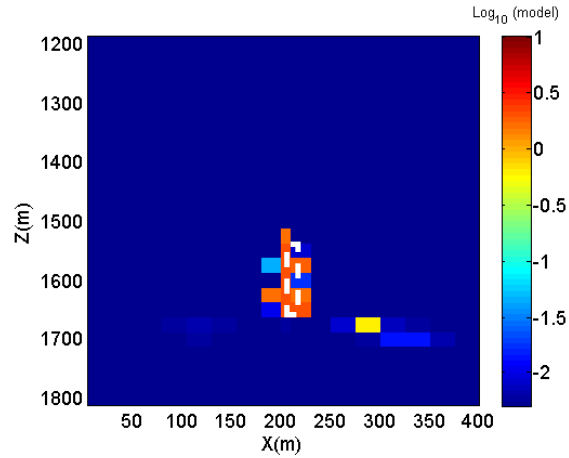


(b)

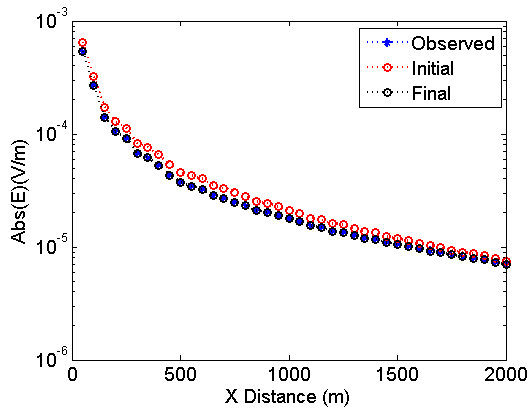
**Figure 11.** Electric field measurements along +x axis (survey line 1) with different background conductivity values. (a) Background conductivity= $5 \cdot 10^{-2}$  S/m. (b) Background conductivity= $5 \cdot 10^{-1}$  S/m. The cased well is coated with 0.2m thick  $10^{-2}$  S/m oil-based mud.



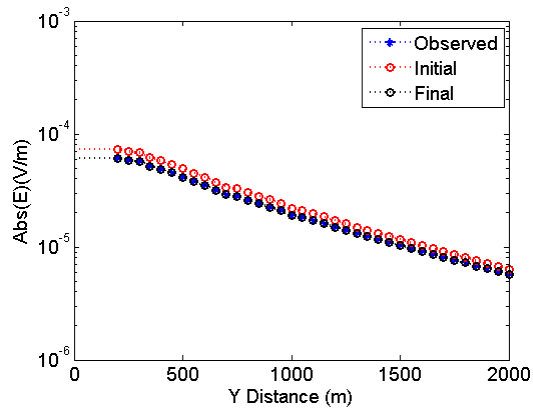
(a)



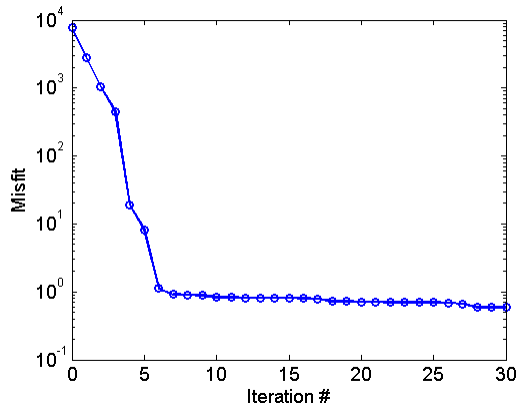
(b)



(c)



(d)



(e)

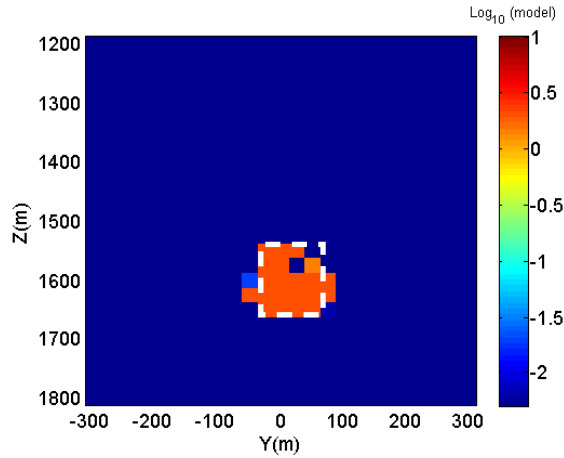
1  
2

3  
4

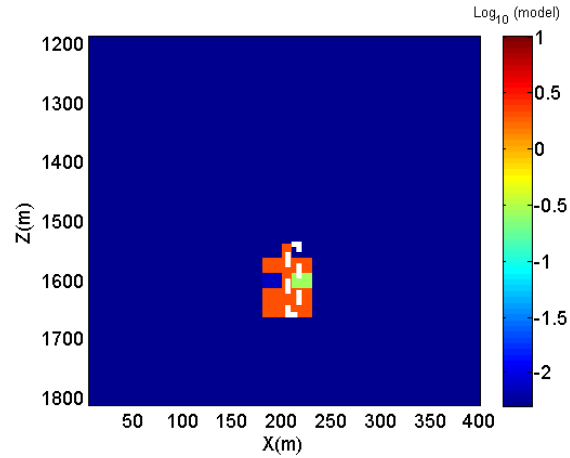
5  
6

7 **Figure 12.** Inversion for model 1. (a)  $YZ$  cross-sectional view at  $x=200\text{m}$ . (b)  $XZ$  cross-sectional view at  
8  $y=0\text{m}$ . (c) Data plots along line 1 before and after the inversion. (d) Data plots along line 2 before and  
9 after the inversion. (e) Misfit as a function of inversion iteration. The white boxes in (a) and (b) indicate  
10 the true boundaries of model 1.

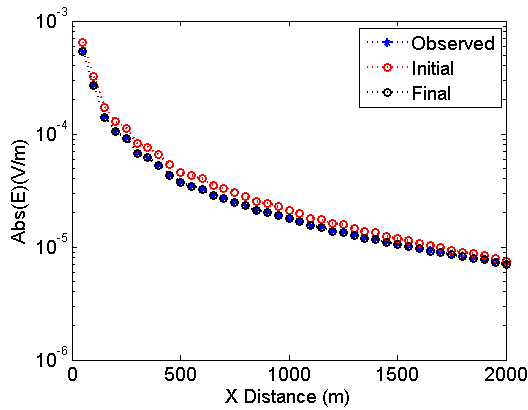




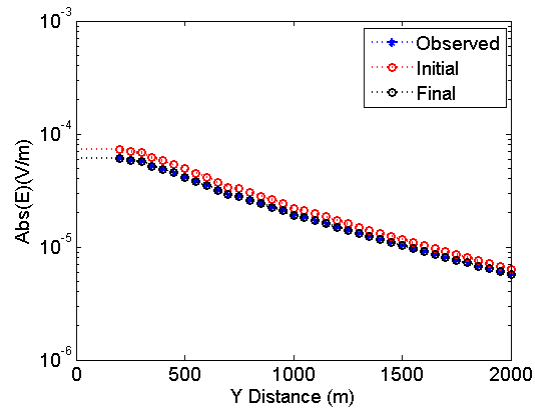
(a)



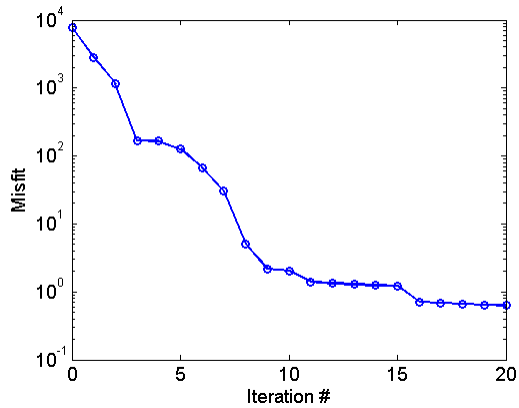
(b)



(c)



(d)



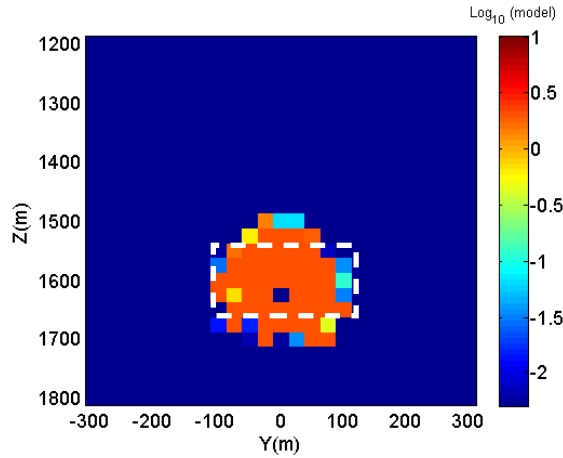
(e)

1  
2

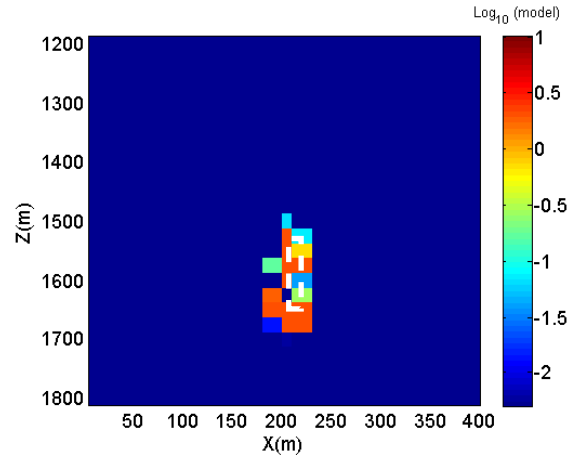
3  
4

5  
6

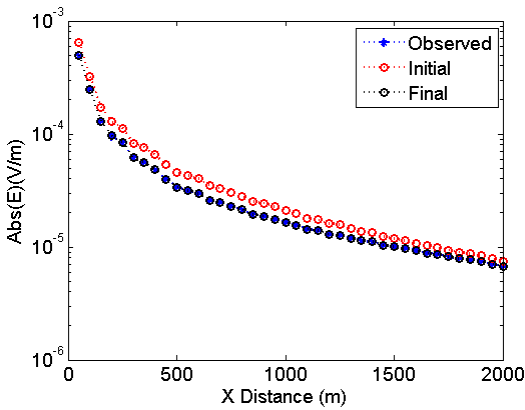
7 **Figure 13.** Inversion for model 1 with the imaging domain constrained in the x-direction. (a) YZ cross-  
 8 sectional view at  $x=200\text{m}$ . (b) XZ cross-sectional view at  $y=0\text{m}$ . (c) Data plots along line 1 before and  
 9 after the inversion. (d) Data plots along line 2 before and after the inversion. (e) Misfit as a function of  
 10 inversion iteration. The white boxes in (a) and (b) indicate the true boundaries of model 1.



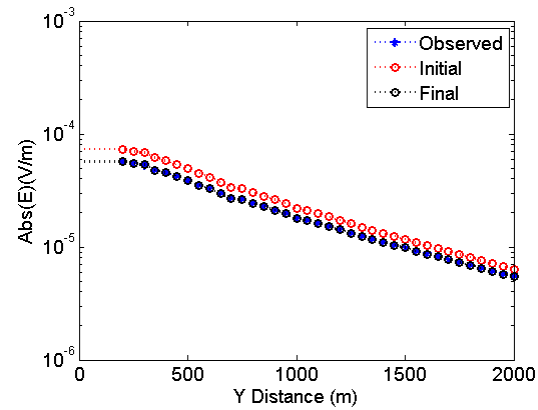
(a)



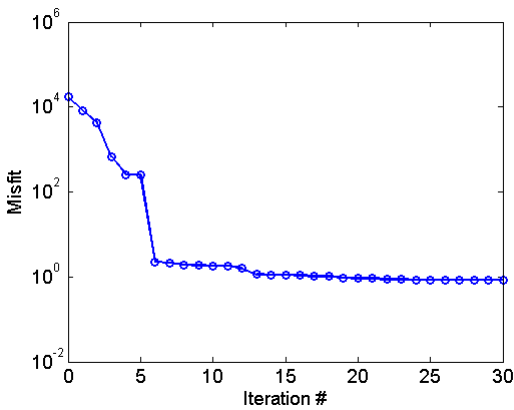
(b)



(c)



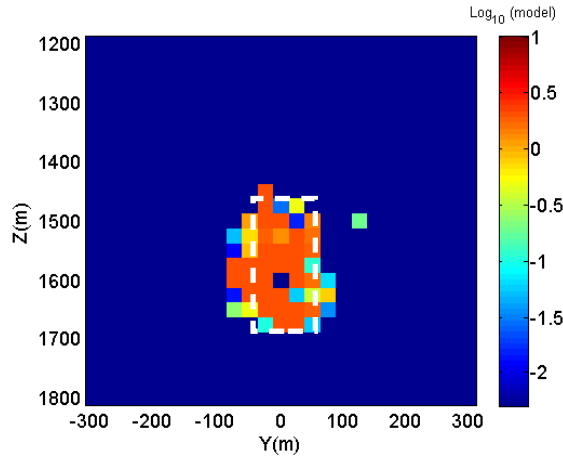
(d)



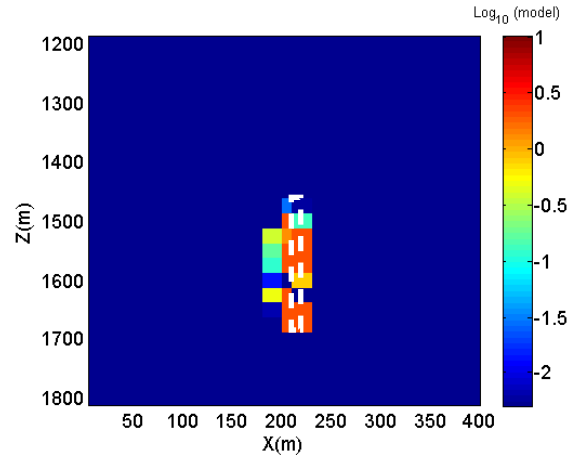
(e)

1  
23  
45  
6

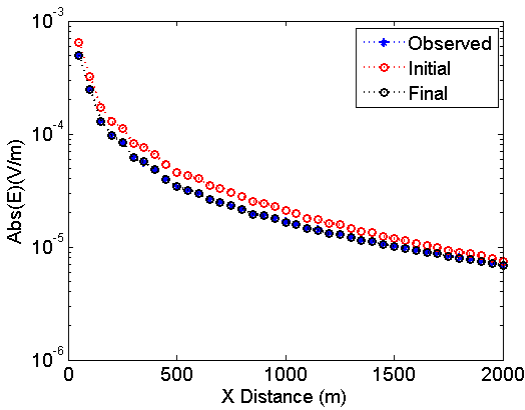
7 **Figure 14.** Inversion for model 2 with the imaging domain constrained in the x-direction. (a) YZ cross-  
 8 sectional view at  $x=200\text{m}$ . (b) XZ cross-sectional view at  $y=0\text{m}$ . (c) Data plots along line 1 before and  
 9 after the inversion. (d) Data plots along line 2 before and after the inversion. (e) Misfit as a function of  
 10 inversion iteration. The white boxes in (a) and (b) indicate the true boundaries of model 2.



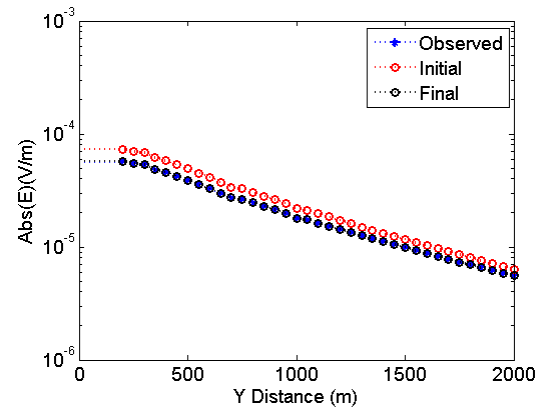
(a)



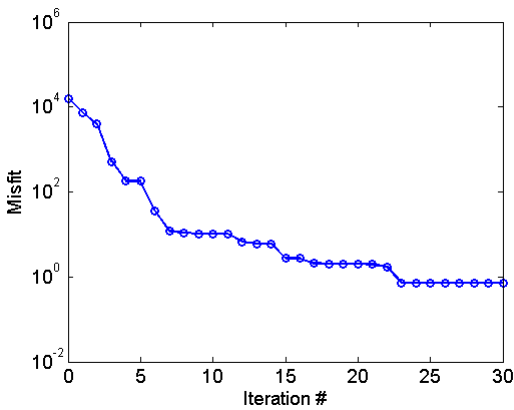
(b)



(c)



(d)



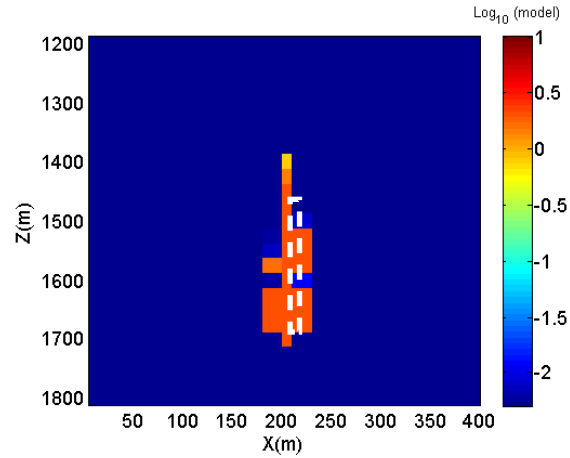
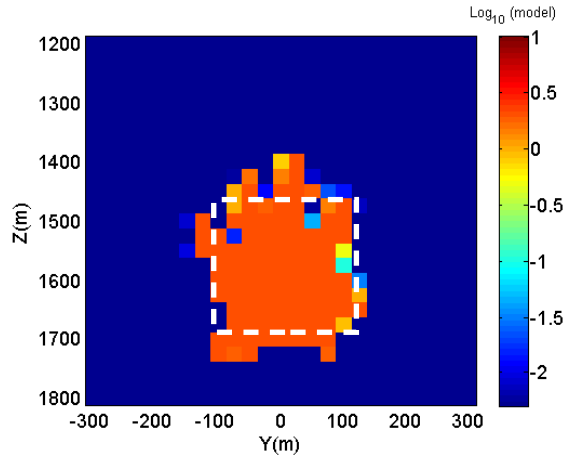
(e)

1  
2

3  
4

5  
6

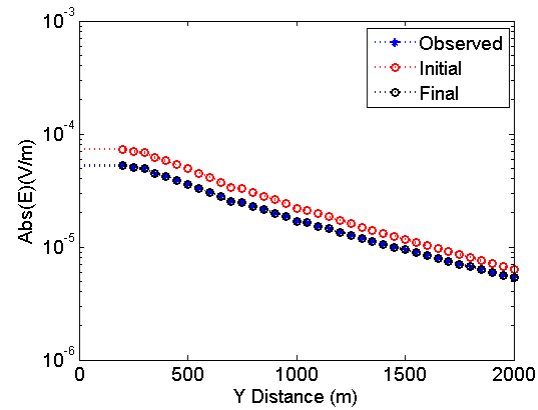
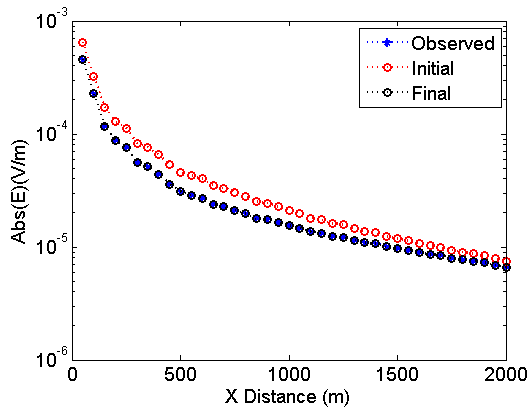
7 **Figure 15.** Inversion for model 3 with the imaging domain constrained in the x-direction. (a) YZ cross-  
 8 sectional view at  $x=200\text{m}$ . (b) XZ cross-sectional view at  $y=0\text{m}$ . (c) Data plots along line 1 before and  
 9 after the inversion. (d) Data plots along line 2 before and after the inversion. (e) Misfit as a function of  
 10 inversion iteration. The white boxes in (a) and (b) indicate the true boundaries of model 3.



1  
2

(a)

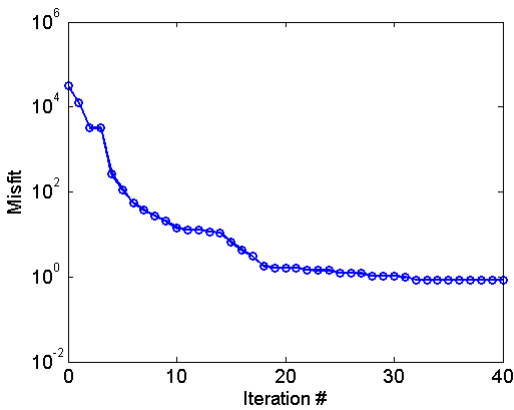
(b)



3  
4

(c)

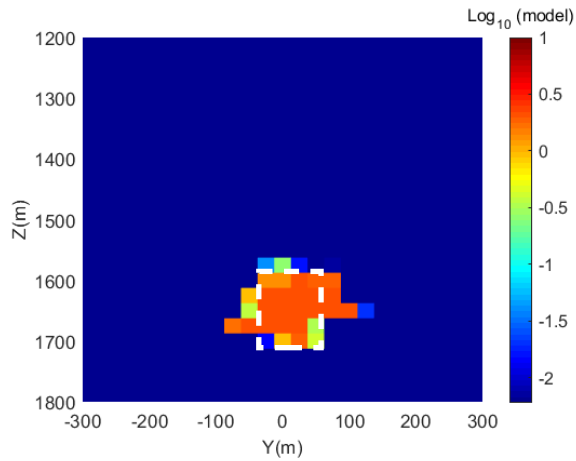
(d)



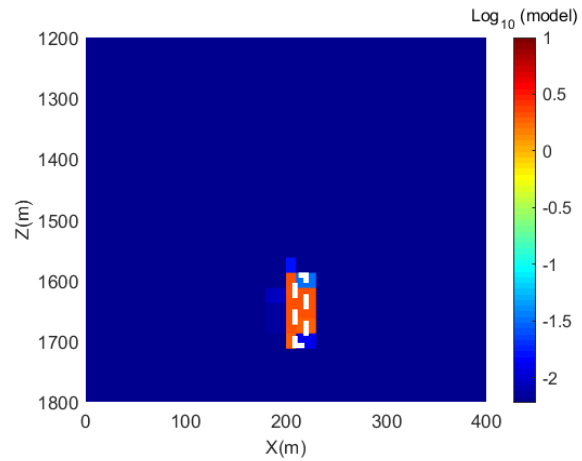
5  
6

(e)

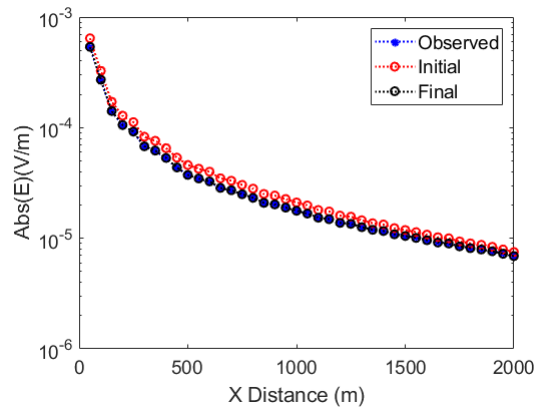
7 **Figure 16.** Inversion for model 4 with the imaging domain constrained in the x-direction.. (a) YZ cross-  
8 sectional view at  $x=200\text{m}$ . (b) XZ cross-sectional view at  $y=0\text{m}$ . (c) Data plots along line 1 before and  
9 after the inversion. (d) Data plots along line 2 before and after the inversion. (e) Misfit as a function of  
10 inversion iteration. The white boxes in (a) and (b) indicate the true boundaries of model 4.



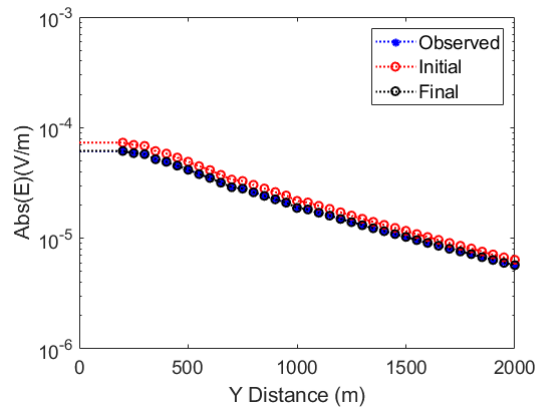
(a)



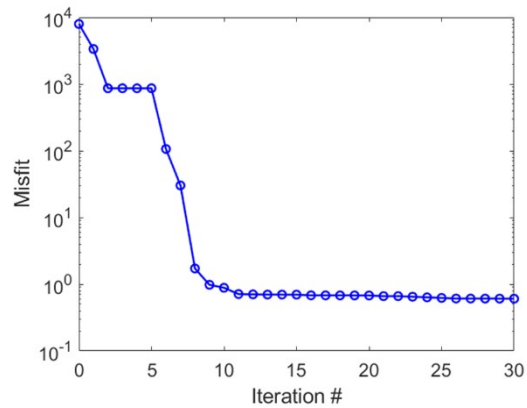
(b)



(c)



(d)



(e)

**Figure 17.** Inversion for model 1 with 5% noise level. (a) YZ cross-sectional view at  $x=200\text{m}$ . (b) XZ cross-sectional view at  $y=0\text{m}$ . (c) Data plots along line 1 before and after the inversion. (d) Data plots along line 2 before and after the inversion. (e) Misfit as a function of inversion iteration.

1 **TABLE CAPTION**

2

HAFZ	Width (m)	Height (m)	Thickness (m)	Conductivity (S/m)
Model 1	$-62.5 \leq y \leq 62.5$	$1537.5 \leq z \leq 1662.5$	$200 \leq x \leq 201$	10
Model 2	$-112.5 \leq y \leq 112.5$	$1537.5 \leq z \leq 1662.5$	$200 \leq x \leq 201$	10
Model 3	$-62.5 \leq y \leq 62.5$	$1462.5 \leq z \leq 1687.5$	$200 \leq x \leq 201$	10
Model 4	$-112.5 \leq y \leq 112.5$	$1462.5 \leq z \leq 1687.5$	$200 \leq x \leq 201$	10

3

4 **Table 1.** The description about the four HAFZ models.